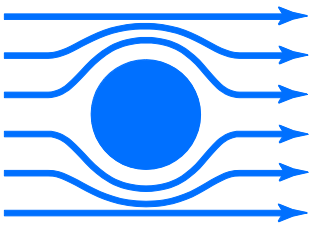

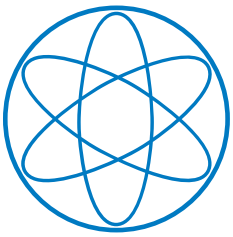

Walther-Meißner-Institut
für
Tieftemperaturforschung

Technische Universität
München

Physik Department
Lehrstuhl E23

Magnetoresistance in the normal and superconducting states of the layered organic metal α-(BEDT-TTF)$_2$KHg(SCN)$_4$ under pressure

Diplomarbeit

Michael Kunz

Themensteller: Prof. Dr. Rudolf Gross
Garching, 28. Oktober 2011

Contents

1 Introduction

One of the major drawbacks for the commercial applications of superconductors up to now is that the superconducting materials currently in use (mainly NbTi and Nb_3Sn for high currents, Nb and Al for sensitive devices) have critical temperatures of $T_c < 20\,\mathrm{K}$. So they need to be cooled down to liquid helium temperatures, which is expensive. These elements and alloys belong to the so-called conventional superconductors, in which Cooper pairs are formed because of electron-phonon interaction, as descibed by the Bardeen-Cooper-Schrieffer (BCS) theory. All elemental superconductors also belong to this class.

Starting with the discovery of the high-T_c superconductors by J. G. Bednorz and K. A. Müller [1] the focus of research has turned to the unconventional superconductors, as they promise superconductivity at far higher temperatures. This class of superconductors includes copper-oxide based materials, heavy-fermion systems, iron pnictides and organic superconductors. First applications with the high-T_c cuprates are already in development [2–4]. Yet also in these compounds the critical temperatures still are not high enough. So a better understanding of the properties of such compounds and of mechanisms responsible for high-T_c superconductivity is desirable in order to produce materials with even higher critical temperatures.

Such superconductors are called "unconventional" as they show different pairing mechanisms than the known electron-phonon interaction and in most cases still are not fully understood. The superconducting state in such materials often shows up in close vicinity to critical points and instabilities like anti-ferromagnetism, transitions of the lattice structure or density wave states. Therefore it seems that competing ground states are often seeds to superconductivity [5]. The transitions between the different ground states can be induced by doping, pressure or magnetic field, depending on the system.

Among these unconventional superconductors are organic charge transfer salts. The highest transition temperature that has been discovered so far, is about 14 K [6]. This is very low compared to the record transition temperatures of high-T_c cuprates or iron pnictides, yet they still are of high interest. In fact one reason for that are the low critical temperatures and low critical fields, since they make it much easier to study the properties of those systems, which are otherwise rather similar to the high-T_c superconductors. The basic structure of such organic charge transfer salts is provided by flat organic molecules, in most cases radical cations. They are packed in stacks or layers, which are separated by inorganic anions, and, therefore, can be considered as quasi-one-dimensional (q1D) or quasi-two-dimensional (q2D) conductors. Because of this reduced dimensionality and a low charge carrier density such compounds show strong electron correlations and several of the above mentioned instabilities. Furthermore, the relative strength of these instabilities can be tuned by slight chemical modifications and in

many cases also by modifications of external parameters like temperature, pressure or magnetic field, which can easily be achieved during experiments.

α-(BEDT-TTF)$_2$KHg(SCN)$_4$ is among the most interesting of these organic charge transfer salts, as it shows the lowest known temperature of a transition into a charge-density wave (CDW) state, at $T = 8$ K, which competes and coexists with superconductivity [7]. At zero magnetic field this CDW state can be suppressed at a critical pressure of $p_c \approx 2.5$ kbar. The behavior of this CDW state at pressures below p_c has already been extensively studied [8–14]. Above p_c, α-(BEDT-TTF)$_2$KHg(SCN)$_4$ is known to enter a field-induced CDW state [11]. A detailed investigation of the properties of the CDW state has been done at the Walther-Meißner-Institut by D. Andres [15]. However, a complete field-temperature phase diagram above the critical pressure of 2.5 kbar does not exist yet. Therefore, in this diploma thesis measurements of the pressure dependence of the effective cyclotron mass of the charge carriers in α-(BEDT-TTF)$_2$KHg(SCN)$_4$ were done. From its behavior some indication of the transition between the CDW state and the normal metallic state in a strong magnetic field was expected.

For pressures above p_c a complete transition into the superconducting state appears at $T \approx 100$ mK [7, 14]. The behavior of this superconducting state was already studied by S. Jakob [16] at the Walther-Meißner-Institut at a pressure of $p = 2.8$ kbar, which is very near to p_c. Thereby a huge polar angle anisotropy of the critical magnetic field was discovered. In this diploma thesis a considerably higher pressure of $p = 3.4$ kbar was applied to the samples in order to investigate how the superconductivity behaves at a pressure farer away from the critical point at p_c. In addition, the behavior of the critical field depending on the polar angle θ was studied at different temperatures. A strong evidence for a paramagnetic pair breaking effect could be obtained, which already had been suggested by S. Jakob, but could not be verified at that time.

Furthermore, the experiments by S. Jakob [16] also showed a considerable inplane anisotropy of the critical field. As the nature of this azimuthal anisotropy remained yet unknown, the effect of pressure to it was investigated in this diploma thesis. To this end, experiments at ambient pressure as well as $p = 3.4$ kbar were carried out.

This Diploma thesis follows the structure given below:

The second chapter of this Diploma thesis introduces the theoretical background describing the behavior of superconductivity and magnetoresistance in layered compounds.

In the third chapter the structure and known properties of the organic metal α-(BEDT-TTF)$_2$KHg(SCN)$_4$ are presented.

The fourth chapter describes the experimental setup used for the measurements of this work.

In the fifth chapter the results of the experiments are presented and analysed. Furthermore, the conclusions drawn from this analysis are discussed and compared to earlier experiments.

A summary of the most important results is given in the sixth chapter.

2 Theoretical background

This chapter summarizes the theoretical background, which is used in this diploma thesis to analyse the experimentally obtained data. As the general properties of superconductors are widely known today, they will not be considered separately here. The only exception is a brief overview of the Ginzburg-Landau theory, since it is the basis for the theories of layered Superconductors. Detailed descriptions of superconductivity can be found for example in [17–19].

2.1 Ginzburg-Landau theory

The Ginzburg-Landau (GL) theory was the first theory of superconductivity capable of describing anisotropic systems. The Cooper pair density is described as a "macroscopic" wave function, the so called order parameter $\Psi(\boldsymbol{r})$. In the GL equations two important characteristic parameters for superconductors are introduced:

1. The GL coherence length

$$\xi_{GL}^2 = \frac{\hbar^2}{4m_e|\alpha|} \tag{2.1}$$

is the characteristic length over which the order parameter can vary and therefore a measure for the size of the Cooper pairs. The temperature behavior follows the relation

$$\xi_{GL}(T) = \xi_{GL}(0)\left(1-\frac{T}{T_c}\right)^{-\frac{1}{2}} = 0.74\xi_0\left(1-\frac{T}{T_c}\right)^{-\frac{1}{2}}, \tag{2.2}$$

where $\xi_0 = 0.18\frac{\hbar v_F}{k_B T_c}$ is the value of the coherence length derived from the BCS-theory[1], v_F is the Fermi velocity and k_B the Boltzmann-constant.

2. The penetration depth

$$\lambda^2 = \frac{m_e c^2 \beta}{8\pi e^2|\alpha|} \tag{2.3}$$

describes the characteristic length over which the magnetic field decays exponentially beneath the surface of the superconductor, with a temperature behavior given by

$$\lambda(T) = \lambda(0)\left(1-\frac{T}{T_c}\right)^{-\frac{1}{2}}. \tag{2.4}$$

α and β are material dependent phenomenological expansion coefficients and m_e is the free electron mass.

[1] The first microscopic theory of superconductivity developed by Bardeen, Cooper and Schrieffer

The GL parameter

$$\kappa = \frac{\lambda}{\xi} \tag{2.5}$$

determines whether magnetic field can penetrate the superconductor via flux vortices above a certain magnetic field or not. In the latter case ($\kappa < 1/\sqrt{2}$) we speak of a type 1 superconductor with a critical field H_{cth}, while $\kappa > 1/\sqrt{2}$ characterizes a type 2 superconductor. In a type 2 superconductor we have a lower critical field H_{c1}, above which the field starts penetrating the superconductor and an upper critical field H_{c2}, above which the superconductivity is completely destroyed. In resistance measurements always H_{c2} is obtained.

For the case of a bulk superconductor H_{c2} is given by

$$H_{c2} = \frac{\Phi_0}{2\pi\xi^2(T)}, \tag{2.6}$$

where $\Phi_0 = \frac{h}{2e}$ is the flux quantum.

2.2 Superconductivity in layered compounds

Most of the unconventional superconductors, which are of current interest, like cuprate, iron pnictide and organic superconductors, are layered materials. Depending on the strength of coupling between the layers such compounds can be either described as highly anisotropic three dimensional (3D) systems or as quasi-two-dimensional (q2D) systems, depending on the ratio of the interlayer coherence length $\xi_\perp$ and the interlayer distance d.

2.2.1 Highly anisotropic superconductors

The description as highly anisotropic 3D systems is used when the perpendicular coherence length $\xi_\perp$ exceeds the interlayer distance d,

$$\xi_\perp > d,$$

meaning that the superconducting layers are still coupled.

The critical magnetic field of layered superconductors is strongly dependent on the polar angle θ between the magnetic field and the conducting planes. For fields perpendicular to the planes the shielding currents are able to flow within the layers and behave normally since the inplane coherence length is rather big. This results in the critical field as a function of temperature $H_{c2,\perp}(T)$ behaving rather similar to bulk superconductors. According to GL theory the temperature dependence of H_{c2} is linear for T near T_c. Werthammer, Helfand and Hohenberg (WHH) [20] have shown that this linear temperature dependence of H_{c2} is valid until much lower temperatures as long as the orbital effect (shielding currents) is responsible for breaking the Cooper pairs. In layered compounds this estimation is generally valid for magnetic fields in perpendicular direction.

For fields parallel to the conducting layers, however, the shielding currents are strongly suppressed, because the transport integral in perpendicular direction is much smaller than the inplane transfer integral $t_\perp \ll t_\parallel$. Therefore the magnetic field can penetrate the superconductor much more easily, resulting in a very low H_{c1}. Because of the very small perpendicular coherence length the flux vortices can be much more densely packed than for perpendicular field. Thus, much higher fields can penetrate the superconductor without destroying the superconductivity resulting in a much higher slope of H_{c2} near T_c. If the slope is very large, the paramagnetic pair breaking mechanism described in section 2.2.3 becomes important.

W. E. Lawrence and S. Doniach have formulated a theory describing layered compounds by individual superconducting planes with a Josephson coupling between the layers [21]. In the case of relatively strong coupling of the layers, they have shown that such superconductors can be described by the anisotropic GL theory for 3D superconductors (equation 2.6), which deviates from the normal GL theory by the introduction of an anisotropic effective mass of charge carriers, $m_\parallel$ and $m_\perp$. According to Lawrence and Doniach the upper critical fields in perpendicular $H_{c2,\perp}$ and parallel $H_{c2,\parallel}$ directions follow the relations:

$$H_{c2,\perp} = \frac{\Phi_0}{2\pi\xi_\parallel^2} \tag{2.7}$$

$$H_{c2,\parallel} = \frac{\Phi_0}{2\pi\xi_\parallel\xi_\perp} \tag{2.8}$$

From that we extract the following equalities [17]

$$\frac{H_{c2,\parallel}}{H_{c2,\perp}} = \frac{\xi_\parallel}{\xi_\perp} = \frac{\lambda_\perp}{\lambda_\parallel} = \left(\frac{m_\perp}{m_\parallel}\right)^{\frac{1}{2}} \equiv \gamma \tag{2.9}$$

introducing a conventional dimensionless anisotropy parameter γ. $\lambda_{\perp,\parallel}$ and $\xi_{\perp,\parallel}$ stand for the parallel or perpendicular component of the penetration depth and the coherence length, respectively.

Therefrom the angular behavior of the upper critical field H_{c2} in highly anisotropic superconductors can be derived:

$$H_{c2}(\theta, T) = \frac{\Phi_0}{2\pi\xi_\parallel^2(T)\sqrt{\gamma^2\sin^2\theta + \cos^2\theta}}, \tag{2.10}$$

with θ being the angle between the magnetic field direction and the conducting layers.

2.2.2 Quasi-two-dimensional superconductors

When the perpendicular coherence length becomes smaller than the interlayer distance,

$$\xi_\perp < \frac{d}{\sqrt{2}},$$

there is no continuous superconducting region throughout the whole superconductor any more. Such a q2D superconductor rather consists of superconducting layers. Therefore

the current perpendicular to the conducting layers is limited to Josephson currents. This results in an even greater angular dependence of the critical field.

R. A. Klemm, A. Luther and M. R. Beasly have analyzed the Lawrence-Doniach model in more detail and developed a theory for the q2D superconductors in the dirty limit [22]. (When the mean free path of a Cooper pair l is much smaller than the coherence length ($l \ll \xi_0$).) For the clean limit ($l \gg \xi_0$) there exists a model proposed by Bulaevskiĭ [23, 24].

Most of the time it is, however, correct to use an easy formula proposed by Tinkham [17] for superconducting thin films and is also valid for the purely 2D case

$$s \ll \xi_\perp \ll d, \tag{2.11}$$

where s is the layer thickness. Under this conditions there is no coupling between the layers any more. The dependence of the critical field on θ now follows the relation

$$\left|\frac{H_c(\theta)\sin\theta}{H_{c\perp}}\right| + \left(\frac{H_c(\theta)\cos\theta}{H_{c\parallel}}\right)^2 = 1, \tag{2.12}$$

with $H_{c\perp}$ and $H_{c\parallel}$ being the critical field in perpendicular and parallel direction to the conducting layers, respectively.

$H_{c\perp}$ is given by Tinkham [17] as

$$H_{c2,\parallel} = \frac{2\sqrt{6}H_{cth}\lambda}{s}. \tag{2.13}$$

Eq. (2.13) can also be written in the form

$$H_{c2,\parallel} = \frac{\sqrt{3}\Phi_0}{\pi s \xi_\parallel(0)}\sqrt{1-\frac{T}{T_c}}. \tag{2.14}$$

This formula was already used to fit data obtained from experiments with q2D layered compounds [25].

As the coherence length $\xi(T)$ increases with temperature and diverges at T_c, all q2D superconductors make a transition into the highly anisotropic 3D state near T_c. In many of them the amplitude and phase of the order parameter has big fluctuations in that regime, which results in rather complex phase diagrams making it difficult to determine their critical fields (see for instance [17] chapter 9).

2.2.3 Paramagnetic pair breaking in layered superconductors

As mentioned above many q2D compounds and to a lower extent also in the highly anisotropic 3D compounds the slope of the parallel critical field near T_c is very huge and for very high fields another pair breaking mechanism becomes dominant. In a magnetic field the electrons gain energy by aligning their spins parallel to the magnetic field because of the Zeeman splitting of energy levels. If we have a s-wave or d-wave superconducting state, however, the Cooper pair electrons have antiparallel spin and therefore they can not all align their spin direction according to the field. If the energy gained by

paramagnetic ordering exceeds the superconducting energy gap Δ_0, the Cooper pairs are broken. This behavior was first theoretically shown by B. S. Chandrasekhar [26] and A. M. Clogston [27]. The paramagnetic critical field H_p shown by the relation

$$\mu_0 H_p = \frac{\Delta_0}{\mu_B \sqrt{2}}, \tag{2.15}$$

with μ_b being the Bohr magneton and μ_0 the vacuum permeability. After inserting $\Delta_0 = 1.76 k_B T_c$ from the BCS theory we get

$$\mu_0 H_p = 1.85 T_c, \tag{2.16}$$

which is called the "Chandrasekhar-Clogston paramagnetic limit" (CC-limit).

According to a theory proposed almost at the same time by P. Fulde and R. A. Ferrell [28] as well as by A. I. Larkin and Y. N. Ovchinnikov [29] superconductivity can survive to even higher magnetic fields under certain conditions. This so called FFLO-state is an inhomogeneous superconducting state, where the Cooper pairs have a finite center of mass momentum ($\boldsymbol{k}\uparrow, -\boldsymbol{k}\downarrow + \boldsymbol{q}\downarrow$). In this state the superconductor has a lower condensation energy than the BCS state, but as the Zeeman energy is reduced in the FFLO state it is stable at sufficiently high fields. Thereby some space of the superconductor is "sacrificed" and becomes normal metallic making it possible for the superconductivity to survive in other parts of the superconductor. For the FFLO state to show up, the compounds must have a Maki parameter $\alpha = \sqrt{2} H_{c2}^{orb} / H_{c2}^{P}$ [30] (ratio of orbital and paramagnetic critical field) higher than 1.8 and it must be in the clean limit ($l \gg \xi_0$).

For these reasons the FFLO state is expected to be largest in 1D superconductors. In 2D superconductors it should be smaller but still visible, while in 3D superconductors the FFLO state is estimated to be very narrow and therefore hard to measure. No clear proof of the existence of the FFLO state has been found yet, but recently there has been evidence for the existence of a FFLO state in q2D organic superconductors [31].

2.3 Magnetoresistance in layered compounds

For understanding the superconducting properties of materials it is also necessary to know the normal state properties. For layered compounds it turned out that the magnetoresistance can give very valuable information. Two important effects that have been studied in this diploma thesis, are magnetic quantum oscillations and angle-dependent magnetoresistance oscillations (AMROs) and will be described in this section. Both of them are powerful tools for studying the Fermi surface (FS) of the compounds. A more detailed description can be found in [32–34].

2.3.1 Magnetic quantum oscillations

When a magnetic field is applied to electrons moving on closed orbits their spectrum becomes quantized. This was first proposed by L. D. Landau [35], who derived the

spectrum of a free electron gas in a magnetic field in the form

$$E(n, k_B) = \left(n + \frac{1}{2}\right)\hbar\omega_c + \frac{k_B^2\hbar^2}{2m_e}, \tag{2.17}$$

where $n = 0, 1, 2, \ldots$, $\omega_c = \frac{eB}{m_e}$ is the cyclotron frequency of a free electron and k_B is the wave vector component parallel to the field $\boldsymbol{B}$.

In **k**-space the allowed electron states are all lying on coaxial tubes parallel to the magnetic field, which are called Landau tubes. With increasing field the Landau tubes' diameter widens, crossing a fixed point in **k**-space periodically in a scale of 1/B, while their degeneracy increases (so that the total number of electrons inside the FS stays constant). The area of the nth landau tube cross section is thereby given by:

$$A_{k,n} = \left(n + \frac{1}{2}\right)\frac{2\pi eB}{\hbar} \tag{2.18}$$

This is the famous Onsager relation [36]. As the Landau tubes cross the FS, the density of states oscillates, which gives rise to the magnetic quantum oscillations measurable in several physical properties. The most important among those are oscillations of the magnetization, first detected by W. J. de Haas and P. M. van Alphen [37], which are therefore called de Haas-van Alphen (dHvA) oscillations, and oscillations of resistance, first discovered by L. W. Shubnikov and W. J. de Haas [38], named Shubnikov-de Haas (SdH) oscillations.

De Haas-van Alphen oscillations

The standard theory for the description of the dHvA oscillations was formulated by I. M. Lifshitz and A. M. Kosevich [39]. They calculated the magnetization as the derivative of the Gibbs thermodynamic potential Ω at constant temperature T and chemical potential μ:

$$\boldsymbol{M} = -\left(\frac{\partial\Omega}{\partial\boldsymbol{B}}\right)_{T,\mu} \tag{2.19}$$

By inserting the thermodynamic potential for the electron states on the Landau tubes one obtains:

$$\tilde{M}_{\parallel} = -\sqrt{\frac{e^5}{2\pi^5\hbar}}\frac{F\sqrt{B}}{m_c|S''|_{\text{extr}}^{\frac{1}{2}}}\sum_{r=1}^{\infty} R_D(r)R_T(r)R_S(r)\frac{1}{r^{\frac{3}{2}}}\sin\left[2\pi r\left(\frac{F}{B} - \frac{1}{2}\right) \pm \frac{\pi}{4}\right], \tag{2.20}$$

where $\tilde{M}_{\parallel}$ is the magnetization parallel to $\boldsymbol{B}$, r the harmonic index, m_c the cyclotron mass and F the fundamental frequency

$$F = \frac{S_{\text{extr}}}{2\pi e\hbar}. \tag{2.21}$$

S_{extr} is the extreme cross section of the FS and $(S'')_{\text{extr}} = (\partial^2 S/\partial p_B^2)_{\text{extr}}$ characterizes the FS curvature along $\boldsymbol{B}$ around the extremal cross section.

Equation 2.20 is called the Lifshitz-Kosevich (LK) formula and describes the dHvA oscillations in a 3D metallic electron system. It contains the damping factors R_D, R_T and R_S describing the effects of finite temperature, scattering effects and Zeeman splitting, respectively. As $R_D(r)$ and $R_T(r)$ decrease exponentially with increasing harmonic index we will only consider the case of the fundamental harmonic, $r = 1$.

Shubnikov-de Haas oscillations

The theory of the SdH oscillations is more complex than that of the dHvA oscillations and still not completely understood. Fortunately, a satisfying description of the SdH oscillations can be usually obtained from Pippard's idea [40, 41] that the scattering probability, hence, the resistivity are proportional to the density of states $D(\mu)$ around the Fermi level. The latter can be shown to be directly proportional to the field-derivative of the magnetization:

$$\tilde{D}(\mu) \propto \left(\frac{m_c B}{S_{\text{extr}}}\right)^2 \frac{\partial \tilde{M}}{\partial B} \tag{2.22}$$

Following from this, the oscillatory part of the conductivity can be expressed in the form

$$\frac{\tilde{\sigma}}{\sigma_0} = a_{r=1} \cos\left[2\pi\left(\frac{F}{B} - \frac{1}{2}\right) \pm \frac{\pi}{4}\right], \tag{2.23}$$

where

$$a_{r=1} \propto \frac{m_c B^{1/2}}{(S'')^{1/2}_{\text{extr}}} R_D R_T R_S \tag{2.24}$$

and σ_0 is the background conductivity.

The damping factors

The temperature damping factor R_T takes into account the temperature-induced smearing of the Fermi distribution function. We can consider this to be electrons with a slight distribution of Fermi energies E_F, which results in slightly different oscillation frequencies. This should lead to smearing of the phase of the oscillations and, therefore, to a decrease of the amplitude. The expression for the temperature damping factor is [39]:

$$R_T = \frac{K m^* \frac{T}{B}}{\sinh(K m^* \frac{T}{B})} \tag{2.25}$$

with the constant

$$K = \frac{2\pi^2 k_B m_e}{\hbar e} \approx 14.7 \frac{\text{T}}{\text{K}} \tag{2.26}$$

and $m^* = m_c/m_e$ being the cyclotron mass normalized to the free electron mass. Thus, the effective mass m^* can be determined by fitting the experimentally observed temperature dependent oscillation amplitude with Eq. (2.25) [32].

The Dingle factor R_D takes into account the broadening of the Landau levels due to imperfections and impurities of the crystal lattice. Assuming this broadening is

described by the Lorentzian distribution function with the half-width $\Gamma = \hbar/2\tau$ (τ being the relaxation time), the Dingle damping factor is expressed by the relation [42]

$$R_D = \exp\left(-Km^*\frac{T_D}{B}\right) \tag{2.27}$$

with

$$T_D = \frac{\hbar}{2\pi k_B \tau} \tag{2.28}$$

which is called the Dingle temperature. After extracting the cyclotron mass m^* from the temperature damping factor the relaxation time can be calculated by fitting the B-dependence by the formula (2.24) with the Dingle factor (Eq. (2.27)).

The spin damping factor R_S, finally, regards the effect of the Zeeman spin splitting. Each Landau level is split into two subbands depending on the electron spin that are separated by the energy gap

$$\Delta E = g\mu_B B, \tag{2.29}$$

where g is the Landé factor ($g \approx 2$ for free electrons) and $\mu_B = e\hbar/2m_e$ is the Bohr magneton. As these two sub bands contribute to the oscillations with the same frequency but with a slightly shifted phase the resulting oscillation amplitude is reduced according to

$$R_S = \cos\left(\frac{\pi}{2}gm^*\right) \tag{2.30}$$

Two dimensional model

In a material with a 3D FS the number of Landau tubes crossing the FS is rather big, resulting in a rather small number of electrons contributing to the oscillations. Therefore, the quantum oscillations are rather small (magnitude of SdH oscillations lies in the order of $10^{-4}\sigma_0$ for $B \sim 10$T). In a system with a 2D Fermi surface the oscillations are much bigger, as there the number of Landau tubes crossing the Fermi surface is rather small (or exactly one in the ideal case) and therefore most of (or in the ideal case all) electrons are contributing to the oscillations (illustrated in figure 2.1).

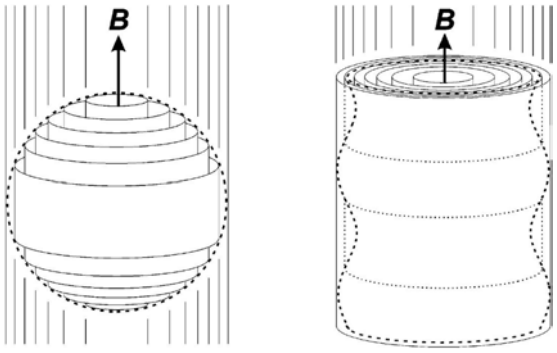

Figure 2.1: Schematic representation of the Landau tubes (thin lines) crossing a 3D isotropic FS (left) and a q2D FS (right) (thick dotted lines) (taken from [33]).

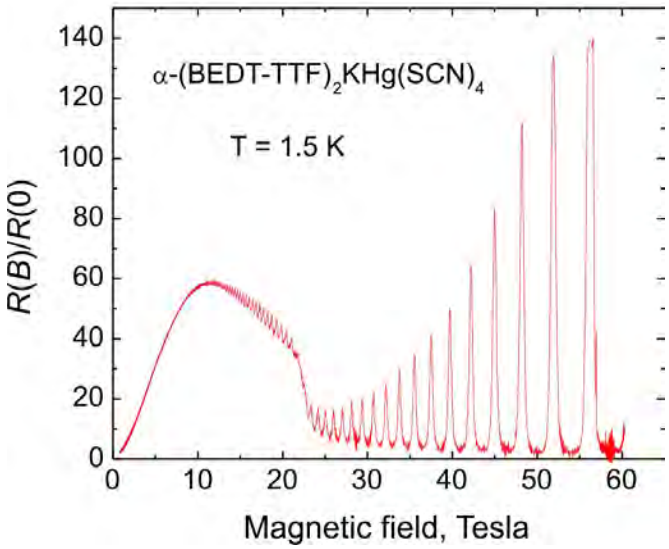

Figure 2.2: Giant SdH oscillations in a sample of α-(BEDT-TTF)$_2$KHg(SCN)$_4$ in pulsed magnetic fields perpendicular to the layers, at $T = 1.5\,\mathrm{K}$ (from M. V. Kartsovnik, private communication).

Naturally, such systems need a theory considering the 2D behavior to be described appropriately. Notably, it has to be considered that as mentioned above a much higher number of electrons are contributing in the oscillations. A modified version of the LK formula for the ideally 2D case (interlayer bandwidth is zero, Landau sub bands are degenerated into sharp levels, all electrons on the FS contributing to the oscillations) has been proposed by Shoenberg [43] for the case of a constant chemical potential $\mu = E_F$. This Lifshitz-Kosevich-Shoenberg (LKS) formula (also known as the 2D LK formula) reads

$$\tilde{M}_{\parallel} = \frac{e}{2\pi^3\hbar}\frac{S}{m_c d}R_D R_T R_S \sin\left(2\pi r\frac{F}{B}\right) \tag{2.31}$$

including the same damping factors as in the 3D case. Here $\boldsymbol{B}$ is supposed to be applied perpendicular to the 2D planes. An important difference to the 2D case is the missing factor $\sqrt{B}$, which should be taken into account when determining the Dingle temperature. This model is only valid for $\hbar\omega_c \gg 2t_\perp$ and weak oscillations.

In figure 2.2 an example of SdH oscillations in α-(BEDT-TTF)$_2$KHg(SCN)$_4$ is shown. As we can see the oscillations are quite small in the field range of our measurements of up to 15 T, so we can assume that the limiting conditions for this model are fulfilled and we, therefore, are allowed to consider only the first harmonic.

2.3.2 Angle-dependent magnetoresistance oscillations

When a magnetic field is applied to a layered compound at different angles with respect to the conducting planes (polar angle θ), oscillations in the resistance $R(\theta)$ can be observed. These so called angle-dependent magnetoresistance oscillations (AMROs)

exist for 1D as well as for 2D electron systems.

In a q1D electron system like the organic TMTSF based compounds, where the conducting chains lie along the x-direction, the dispersion relation follows the expression

$$E(k) = \hbar v_F(|k_x| - k_F) - \sum_{m,n} t_{mn} \cos(m a_y k_y + n a_z k_z) \tag{2.32}$$

with the transfer integrals $t_{mn} \ll E_F$ and $a_{y,z}$ the lattice constants perpendicular to the chains. For such electron systems different kinds of oscillating phenomena can be observed. We will, however, lay our focus on the Lebed Magic-Angle (LMA) resonances:

A. G. Lebed first predicted that the resistivity perpendicular to the highly conducting chains should show peaks at angles following the relation [44]

$$\tan \theta_{\mathrm{LMA}} = \frac{p}{q} \frac{a_y}{a_z}, \tag{2.33}$$

where p and q are integers. It was later shown that the resistance in fact has dips at the LMAs. There are several models trying to explain this behavior, the most popular of which was proposed by T. Osada et al. [45] and interpreted qualitatively by M. V. Kartsovnik et al. [46]:

Under a magnetic field the electrons move in k-space in the direction perpendicular to the field. This makes the electrons' velocity components in k_z and k_y directions, given by $v_{y,z} = \partial E / \hbar \partial k_{y,z}$, oscillate. The mean velocity $\overline{v_{y,z}}$ is given by an average over the scattering time τ. Assuming a large τ for most field angles the electrons' trajectories will cover the whole reduced Brillouin zone (BZ), as can be seen in figure 2.3 (a), thereby occupying all possible nonequivalent k-states on the FS. In that case $\overline{v_{y,z}}$ becomes vanishingly small at $B \to \infty$. This results in the resistance increasing with B. If the trajectories, however, are oriented in a direction described by the reciprocal lattice vector $\boldsymbol{K} = p\boldsymbol{K}_y + q\boldsymbol{K}_z$ only few paths of the reduced BZ are covered as long as p and q are small, as illustrated in figure 2.3 (b). Therefore $\overline{v_{y,z}}$ maintains a finite value and the resistance remains constant at increasing B.

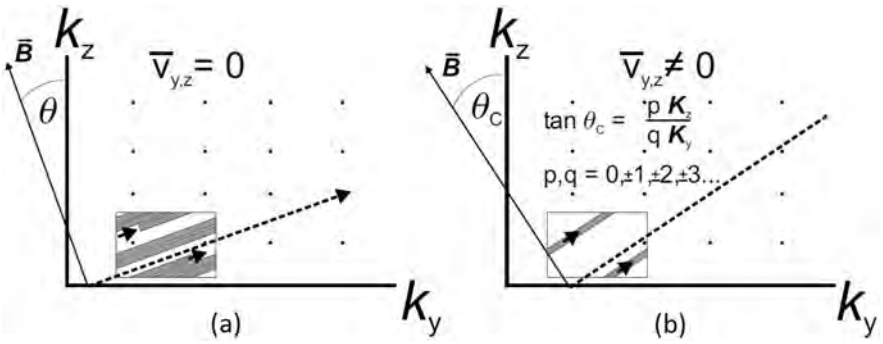

Figure 2.3: Due to the Lorentz force in magnetic field electrons move along the open sheets of the FS lying in the $k_y k_z$-plane. (a) If the trajectory does not run along a reciprocal lattice vector the electron path covers all nonequivalent k-states (i.e. all states in the reduced BZ). (b) Otherwise the trajectory only consists of a few lines on the FS (taken from [15]).

In a q2D systems like α-(BEDT-TTF)$_2$KHg(SCN)$_4$, which possess open FS sheets and in addition have a high anisotropy between y- and z-direction, Eq. (2.33) can be simplified to the case of $q = 1$:

$$\tan \theta_{\mathrm{LMA}} = p\frac{a_y}{a_z} \tag{2.34}$$

Furthermore in the AMRO spectrum shows a strong dependence on the azimuthal angle φ for all LMA.

This model may be qualitatively correct and gives a correct prediction for the values of LMA. However, it has difficulties in reproducing the experimentally obtained magnitude of AMRO and some other fine details of angle-dependent magnetoresistance. There are several newer models [47–49], which are too complicated to be shown in this thesis, however, the mechanism is qualitatively the same.

3 The organic metal α-(BEDT-TTF)$_2$KHg(SCN)$_4$

3.1 Synthesis

Crystals of α-(BEDT-TTF)$_2$KHg(SCN)$_4$ (BEDT-TTF stands for bis(ethylenedithio)-tetratiafulvalene) are grown by electrochemical methods [50, 51]. The molecules BEDT-TTF, KSCN and Hg(SCN)$_2$ are dissolved in a mixture of (1,1,2)trichloroethane and methanol. By applying a constant current using two Pt-electrodes the BEDT-TTF molecules are electrochemically oxidized. Thereby the solved salts serve as electrolytes. The solution then is left for a few weeks at a constant temperature of 20°C and a very low current density of 1-2 mA/cm^2 until small plate-like samples with a typical size of 0.5*0.5*0.1 mm^3 appear on the Pt-anode. The samples for the present experiments were provided by H. Müller[1] and N. Kushch[2].

3.2 Crystal structure

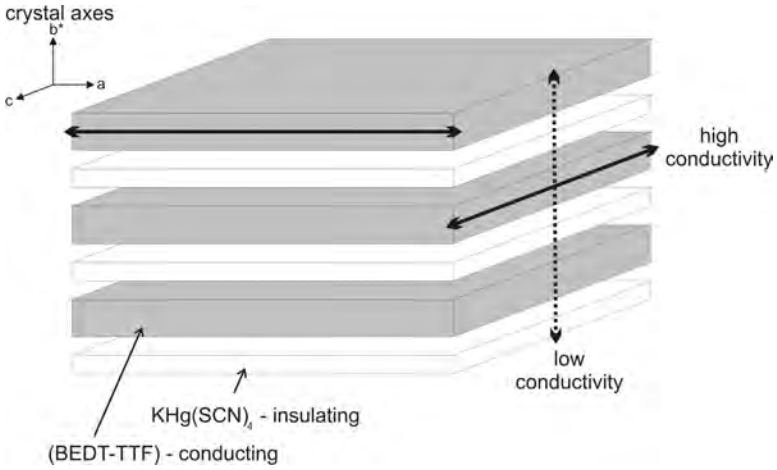

Figure 3.1: Schematic view of the layered structure of α-(BEDT-TTF)$_2$KHg(SCN)$_4$ ([16])

A crystal of α-(BEDT-TTF)$_2$KHg(SCN)$_4$ consists of two kinds of layers stacked onto one another. The layers lie parallel to the a-c plane as sketched in Fig. 3.1. The

[1]European Synchrotron Radiation Facility, 38043 Grenoble, France
[2]Institute of Problems of Chemical Physics, 142432 Chernogolovka, Russian Federation

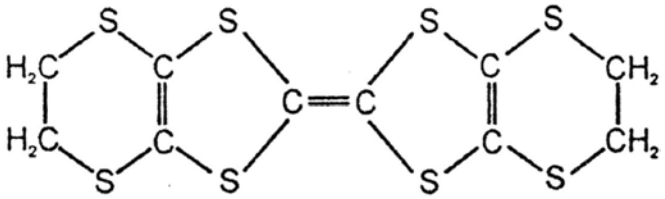

Figure 3.2: Schematic of the molecule BEDT-TTF, which forms the radical cation in the charge transfer salt α-(BEDT-TTF)$_2$KHg(SCN)$_4$ (taken from [52])

inorganic anions $KHg(SCN)_4^-$ form an insulating layer, while the layers consisting of the organic radical cation BEDT-TTF are conducting.

The BEDT-TTF molecules, which are schematically illustrated in Fig. 3.2 are plate-like (2D) in appearance. They donate electrons to anionic $KHg(SCN)_4$ thereby binding the layers together. For that reason these materials are called charge transfer salts.

In the insulating layers the SCN groups form a bridge between the K^+ and Hg^{2+} cations forming a polymeric network in the a-c plane. The BEDT-TTF molecules are connected via the π-orbitals, which are also responsible for the high inplane conductivity of the crystal. The long axes of the BEDT-TTF molecules are oriented almost perpendicular to the layers as illustrated in Fig. 3.3 (a), while the short axes are oriented in a fish bone pattern as shown in Fig. 3.3 (b). This specific pattern is called the

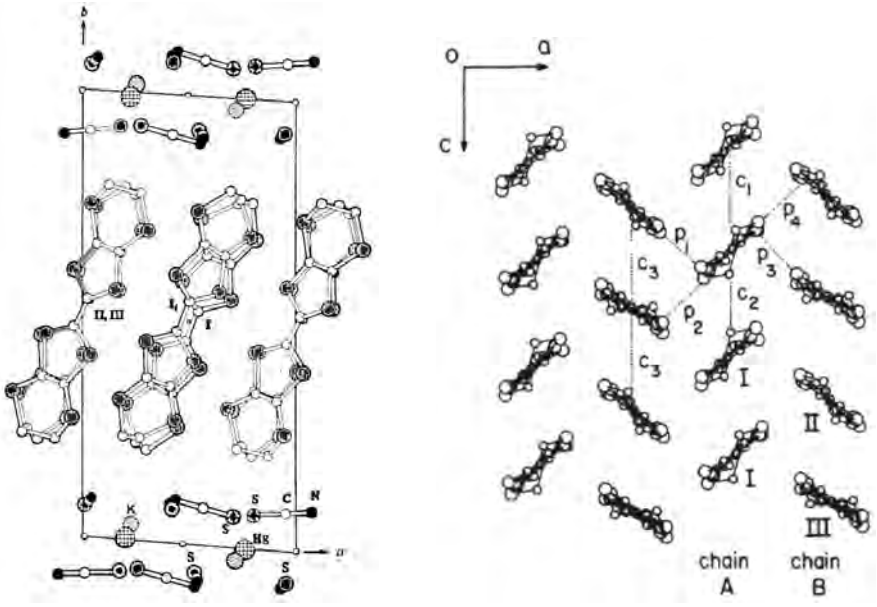

(a) (b)

Figure 3.3: Structure of α-(BEDT-TTF)$_2$KHg(SCN)$_4$ projected along (a) the c-direction and (b) along the b-direction. Transfer integrals along the stack direction and in between the different stacks are denoted by c_i and p_i, respectively (both from [50]).

α-phase.

The crystal structure is triclinic with the parameters a = 1.0082 nm, b = 2.0565 nm, c = 0.9973 nm and the angles $\alpha = 103.7°$, $\beta = 90.91°$, $\gamma = 93,06°$, resulting in a total volume of 1.997 nm^3 for the unit cell [50].

3.3 Band structure and electronic properties

As we have seen in section 3.2 the chemical structure of α-(BEDT-TTF)$_2$KHg(SCN)$_4$ is rather complicated. Its electronic system, however, is quite simple. In Fig. 3.4 the band structure of α-(BEDT-TTF)$_2$KHg(SCN)$_4$ is shown. It was calculated by Mori et al. [53] using the extended Hückel tight-binding model. Newer first-principles calculations have not yielded dramatically different results [54].

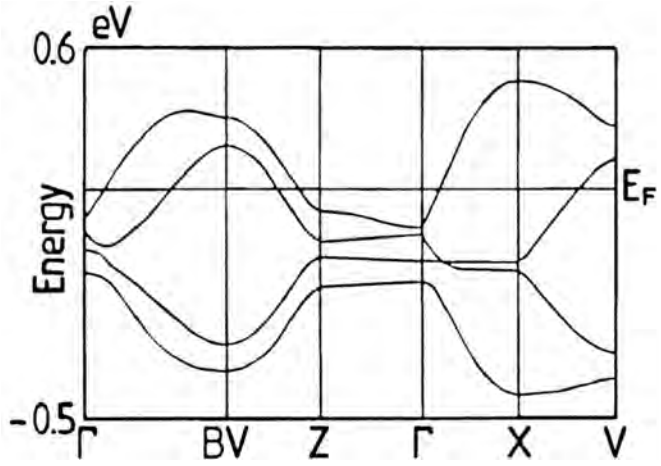

Figure 3.4: Band structure obtained from extended Hückel tight-binding theory for α-(BEDT-TTF)$_2$KHg(SCN)$_4$ at T = 100 K (taken from [53]).

In α-(BEDT-TTF)$_2$KHg(SCN)$_4$ we have four BEDT-TTF molecules per unit cell. Therefore, there exist four HOMO (=highest occupied molecular orbital) levels, one for each molecule. As every two BEDT-TTF molecules donate one electron to the anionic layer, leaving holes behind, we have two holes h^+ per unit cell, which means that six electrons remain. Because two of the HOMO levels overlap in energy scale, we have two half filled bands (two bands crossing the Fermi level), resulting in a metallic character of α-(BEDT-TTF)$_2$KHg(SCN)$_4$. The molecular orbitals of the neighboring layers overlap only slightly, but the conductivity in the direction perpendicular to the layers is still finite.

The anisotropy of the resistivity due to the layered structure of α-(BEDT-TTF)$_2$ KHg(SCN)$_4$ at room temperature is

$$\frac{\rho_\perp}{\rho_\parallel} > 10^4. \tag{3.1}$$

The ratio of the effective transfer integrals within and across the layers was calculated from magnetoresistance behavior to approximately 500 [55], being one of the highest

among the known organic conductors. Nevertheless, the temperature dependence of the resistivity in both directions shows a metallic character upon cooling at low temperatures. At high temperatures in contrast the temperature dependence of resistivity shows a negative slope. The extremely high anisotropy leads to the fact that even at low temperatures the interlayer transport can be coherent or incoherent, depending on the sample quality. This in particular manifests in distinct features in the high field magnetoresistance, as discovered recently [55, 56].

From the calculated band structure the inplane Fermi surface (FS) of α-(BEDT-TTF)$_2$KHg(SCN)$_4$ can be derived, which can be seen in Fig. 3.5. The FS consists of a closed cylindrical part, responsible for the (q)2D properties of the electron system like, for example, the magnetic quantum oscillations. The open sheets account for (q)1D properties including the formation of a charge density wave state, which is introduced in section 3.4. Experiments have shown that this FS can be referred to as q2D, as it is only slightly warped in the perpendicular direction along the b-axis (perpendicular to the layers), following from the finite dispersion between the planes.

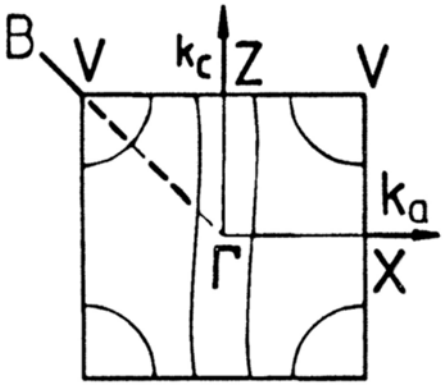

Figure 3.5: 2d Fermi surface calculated for α-(BEDT-TTF)$_2$KHg(SCN)$_4$ using the crystal parameters at T = 100 K (taken from [53]).

By using the SdH and dHvA oscillation frequency the area of the cylindrical FS parts can be evaluated to $\sim$ 15.5% of the cross section of the Billouin zone. The Fermi temperature was determined to $T_F \approx 300\,\mathrm{K}$ [52].

3.4 Phase diagrams

α-(BEDT-TTF)$_2$KHg(SCN)$_4$ undergoes a transition into some kind of density wave state at a transition temperature of $T_K = 8$ K, first reported by Sasaki et al. [57] and later by some other groups [8, 58]. Nowadays this density wave state is generally agreed to be a charge density wave (CDW) [11, 15, 59]. The transition temperature is the lowest for any known system forming a CDW state and therefore allows experimental studies over a large part of the phase diagram by modulating pressure, temperature and magnetic field.

The CDW is a kind of Peierls-transition as predicted for 1D electron systems and can be seen in several organic metals as well as in some inorganic compounds. It appears

in systems that feature an instability against nesting of the q1D part of the FS. This is the case if parts of the FS can be translated onto another part by a single wave vector, the so-called nesting vector $\boldsymbol{Q}$. In the present compound this nesting leads to a reconstruction of the FS with new closed orbits and new open sheets running in the direction of the nesting vector, which is tilted at an angle of 20° from the c-axis according to AMRO measurements [34, 46]. The value of this angle, however, is still subject of discussion as other groups have derived slightly different angles from their measurements [60, 61].

3.4.1 T-p phase diagram

Let us first look at the case without magnetic field ($B = 0$): Here α-(BEDT-TTF)$_2$ KHg(SCN)$_4$ features a CDW state with a fully gapped q1D FS at ambient pressure. However, it can be influenced by applying hydrostatic pressure to the samples as was shown by D. Andres et al. [7, 15]. The nesting conditions of the compound change with increasing pressure due to an increasing overlap of the molecular orbitals resulting in a change of the transfer integrals and therefore also of the FS. At pressures above a "critical pressure" of $p_c \approx 2.5$ kbar the open sheets cannot be nested any more and the CDW state is suppressed.

α-(BEDT-TTF)$_2$KHg(SCN)$_4$ also features a superconducting state. Below 2.5 kbar the superconducting state has a onset temperature of ≈ 300 mK. However the resistance does not drop to zero. Therefore a coexistance of the CDW and superconductivity is assumed, with the superconducting state being present only in small regions or filaments. Above 2.5 kbar the compound shows a sharp transition from the normal metallic to completely superconducting state at temperatures $T_c \approx 100$ mK. T_c decreases further

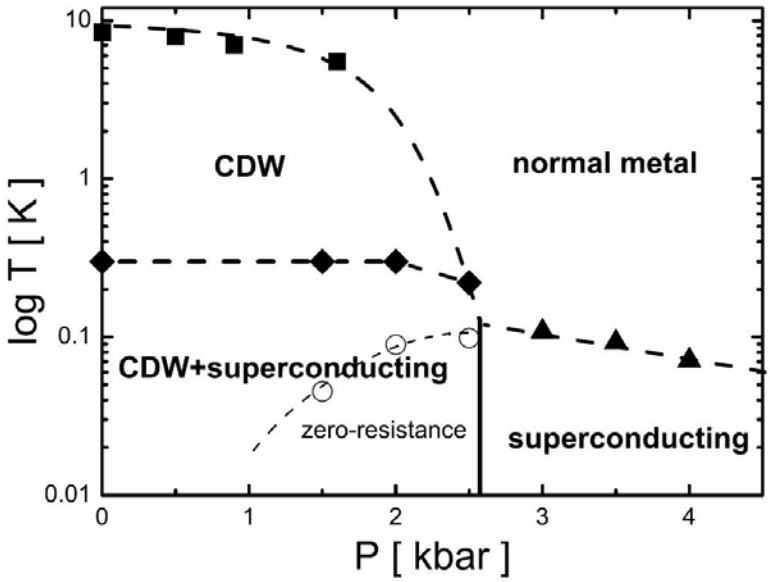

Figure 3.6: T-p phase diagram of α-(BEDT-TTF)$_2$KHg(SCN)$_4$ (taken from [15]).

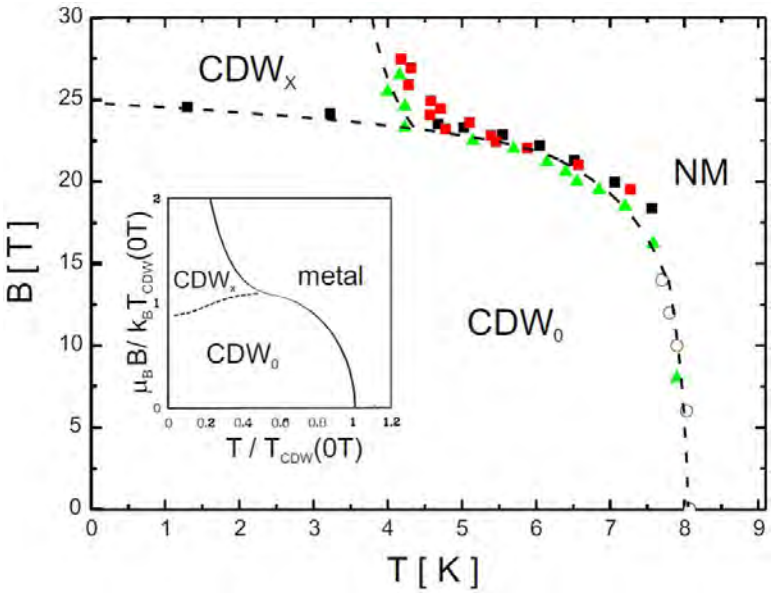

Figure 3.7: B-T phase diagram of α-(BEDT-TTF)$_2$KHg(SCN)$_4$ (taken from [15]). Inset: Theoretically determined phase diagram for a fully gapped CDW$_0$ state proposed by McKenzie [62] and Zanchi et al. [63]

with increasing pressure with a rate of ≈ 30 mK/kbar. The whole p-T phase diagram is shown in Fig. 3.6.

3.4.2 B-T phase diagram

CDW state

Applying a magnetic field also influences the nesting conditions. Above a critical field B_k the nesting becomes imperfect and the system changes from a normal charge-density wave state (CDW$_0$) into a CDW$_x$ state with a modulated order parameter undergoing a field induced phase transition that is expected to be of first order. The CDW$_x$ in fact is a mixed CDW and SDW state with a nesting vector expanded along the conducting chains. This state is analogue to the FFLO state for superconductivity described in section 2.2.2 and is expected to remain present up to much higher fields than the fully gapped CDW$_0$ state. The transition between the charge-density wave states and the normal metallic state is always of second order. The T-B phase diagram at ambient pressure is given in Fig. 3.7.

The pressure dependence of the phase diagram was studied by D. Andres [13] and shows very surprising results. As we know from Fig. 3.6 the transition temperature of the CDW state decreases by applying pressure, but as shown in Fig. 3.8 applying magnetic field shifts the transition temperature back to higher values (see for instance Fig. 3.8, curve for $p = 2.3$ kbar). And even when the CDW is completely suppressed ($p > p_c \approx 2.5$ kbar) a magnetic field can induce a CDW state. This behavior is now well understood and is explained by the stabilization of a CDW by the orbital effect

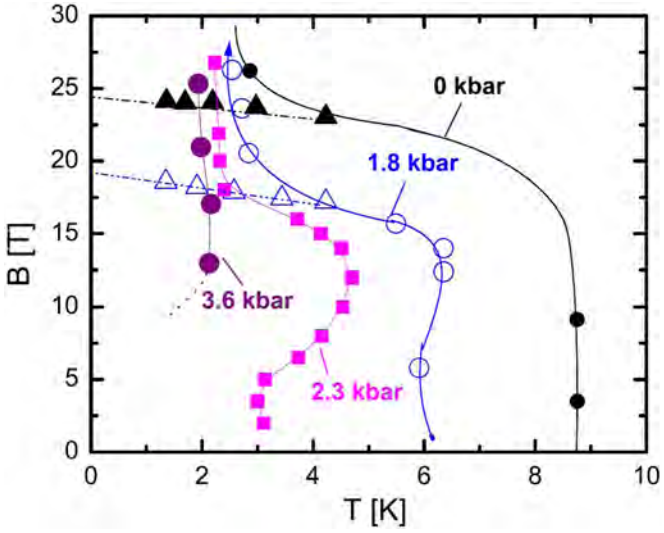

Figure 3.8: Phase transition between CDW state and normal metallic state at different pressures (taken from [15]).

(Zanchi et al. [63]). For the case $p > p_c$ the the theory predicts a cascade of transitions the so called field induced CDW (FICDW) transitions. The behavior of the pressure dependent phase boundary between the FICDW state and the normal metallic state at such pressures, especially at low temperatures, and the pressure, where also the FICDW state is completely suppressed, has not yet been determined reliably.

Superconducting state

The properties of the superconducting state in magnetic fields were already investigated by D. Andres and S. Jakob. D. Andres [7] studied in detail the pressure dependence

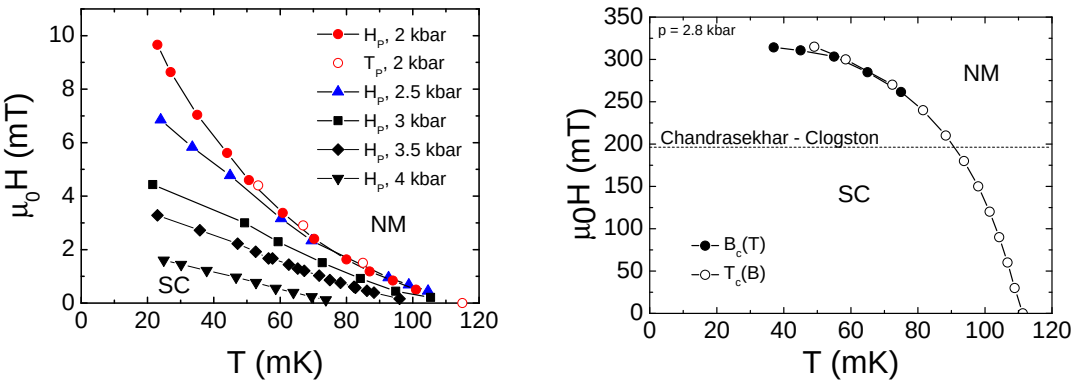

(a) (b)

Figure 3.9: (a) Dependence of $H_{c2,\perp}$ on temperature at different pressures (taken from [7]) (b) Dependence of $H_{c2,\parallel}$ at $p = 2.8$ kbar (taken from [16])

of the perpendicular critical field. His results are given in Fig. 3.9 (a). As we can see, above the critical pressure the perpendicular critical field has a linear temperature dependence following the above mentioned WHH-model [20]. So we can be sure that in the perpendicular direction the orbital pair breaking effect is responsible for the destruction of the superconducting state.

S. Jakob [16] studied the anisotropy of the critical fields at a pressure of 2.8 kbar, just above the critical pressure. In Fig. 3.9 (b) the upper critical field for a direction parallel to the layers is shown. There still is a linear dependence near T_c, at lower temperatures, however, the critical field tends to saturation. Thereby the CC-limit given in Eq. (2.16) is exceeded by a factor of more than 1.5 [16]. This is not due to the fact that there is no paramagnetic effect in α-(BEDT-TTF)$_2$KHg(SCN)$_4$. The reason for the exceeding of the CC-limit is likely an enhanced energy gap (compared to the BCS value) due to many-body interactions. Therefore we refer to it as the paramagnetic limit for α-(BEDT-TTF)$_2$KHg(SCN)$_4$ from here on. The existence of the paramagnetic limit is strongly suggesting a pair breaking due to Pauli-paramagnetism. Because of that the superconductivity in this region is of singlet type [16] as for a triplet superconductor there exists no paramagnetic limit.

4 Experimental setup

In this chapter the setup of the experiments is described. In general two experimental setups were used: One for the effective mass measurements in high magnetic fields and at ^{4}He temperatures and one for the main measurements in a dilution fridge using a vector magnet.

4.1 Setup for effective mass measurement

This section describes the experimental setup used for the effective mass measurement, which was done using the clamp cell technique to create high pressures. A 15T superconducting magnet cryostat together with a variable temperature insert (VTI) were used to apply high magnetic fields and control temperature.

4.1.1 Superconducting magnet

For applying steady magnetic fields of up to 15T, a superconducting magnet from Cryogenics was used. The magnet consists of two different superconducting coils (the inner coil consists of Nb_3Sn and the outer coil of NbTi) which are mounted coaxially and coupled in series. The coils are cooled by the liquid ^{4}He bath in the cryostat which surrounds the coils completely. For applying magnetic fields the magnet coils are connected to an external power supply, in our case an "Oxford IPS 120-10", which is able to apply currents up to 120A.

4.1.2 Temperature controlling

For this experiment smooth controlling of the temperature between 6 K and 1.4 K was needed. To achieve this in the helium bath of the magnet a VTI was used. The VTI consists of two coaxial tubes with some space in between that can be either evacuated or filled with exchange gas in order to optimize the thermal coupling of the sample space with the environment. On the bottom of the VTI a capillary with a rather high impedance connects the sample space with the helium bath, as can be seen in Figure 4.1. When the sample space of the VTI is pumped, a constant helium flow enters the VTI. By regulating the pressure,

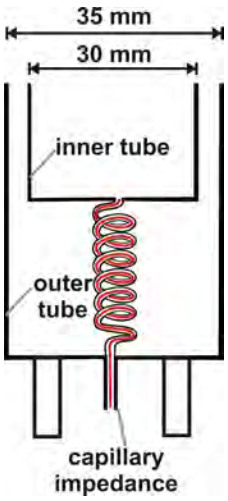

Figure 4.1: Principle sketch of the lower part of the VTI with the Impedance (taken from [64]).

temperatures between 1.4 K and 4.2 K can be stabilized without heater according to the pressure dependent boiling temperature of ^{4}He. For temperatures above 4.2 K a heater must be used. That way stable temperatures up to 80 K can be achieved.

The temperature was measured with a Cernox resistor attached to the outside of the pressure cell, which was read out by a "Lake Shore 340" temperature controller. When heating was necessary, the heater was also controlled by the Lake Shore device. Because of the, however weak, magnetoresistance of the Cernox the temperature value derived from the pressure in the sample space was deemed to be more reliable and therefore it was always used in the temperature range below 4.2 K.

4.1.3 Clamp Cell

To apply pressure the samples were mounted inside a clamp pressure cell. A picture of the clamp cell used can be seen in Figure 4.2. The cell is made of CuBe. One end is sealed by a feed-through, also made of CuBe that contains copper wires embedded in "Stycast"-epoxy, which are used for the measurements inside the cell. On top of the feed through one or two samples and a manganin coil were connected via 20 μm platinum wires.

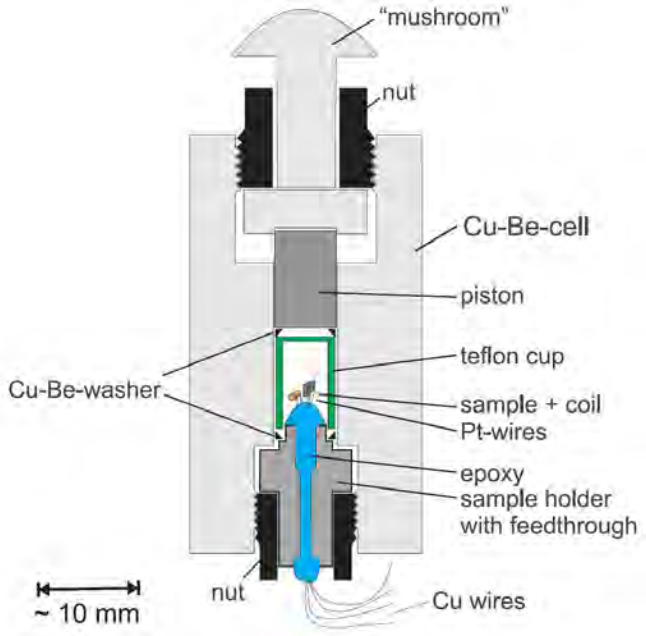

Figure 4.2: Schematical drawing of a clamp cell (taken from [15])

Pressure is applied by a piston made of tungsten carbide, which is pressed on the Teflon cup that is filled with a liquid pressure medium. During the effective mass measurement the silicon oil "GKZh" was used, which is suitable because it has a very low compressibility and solidifies at about 150-220 K (depending on pressure) with a rather small volume effect. As it forms an amorphous structure it provides a rather isotropic pressure even at low temperatures. The piston is held in place by a CuBe

plate which itself is fixed by the nut. When pressurizing the cell, at first force is applied on the steel mushroom by a hydraulic press and then the nut is screwed tight in order to keep the pressure. When the final pressure is reached and the nut is tightened the force on the mushroom can be released.

Between the Teflon cup and the feed through as well as between the cup and the piston there are two CuBe washers, which are sealing the pressure space and prevent the Teflon from floating.

To measure the pressure inside the cell a manganin coil is used. Manganin is suited for that purpose as its resistance has a nearly linear pressure dependence. The resistance change by $\sim 0.25\%$ per kbar is not very high resulting in a pressure uncertainty of at least ± 150 bar. At first a dependence measured by Dieter Andres [15] was used. But since it could not be determined with certainty if the measured pressure values were correct the manganin coil used in the clamp cell was later calibrated using a gas-pressure system. This gas pressure system was originally assembled by D. Andres and is described in [15]. It was not used for these effective mass measurements, because of leakage problems. With this clamp cell up to 10 kbar at room temperature (about 8 kbar at low temperature) were applied in this experiment.

4.1.4 Measurement of sample and manganin resistance

The resistance of the samples was measured by lock-in amplifiers "Stanford Research Systems DSP model SR 830". To make a correct measurement of the sample resistance without measuring the contact and lead resistances the four probe technique was used: Two pairs of contacts were glued to the sample using graphite paste. The contacts of each pair were placed on opposite sides of the sample with the current perpendicular to the conducting a-c plane (as seen in Figure 4.3).

One pair of contacts was connected to the oscillator of the lock-in amplifier through a box containing a high-ohmic resistor, which is used to keep the current stable, and a reference resistor, which is used to measure the current through the sample when connected to the lock-in's input instead of the sample (which can be achieved by the two switches seen in Figure 4.3). Both resistors are placed in series with the sample. The value of the high ohmic resistor is chosen high enough that the sample resistance and the reference resistor can be neglected when calculating the current. In our experiment the oscillator voltage was set to 1 V with a resistor of $100\,\mathrm{k}\Omega$ resulting in a current of $10\,\mu\mathrm{A}$. The oscillator frequencies were set to 20 Hz and 79 Hz respectively.

In the clamp cell the manganin coil inside the cell is used to estimate the pressure. Therefore the manganin resistance was always measured during loading at room temperature and during cooling and warming of the cell (between room temperature and low temperature). The value for the pressure at low temperatures was taken at 15 K. For measuring the manganin resistance a "Keithley 2400 SourceMeter" and a "Keithley 2000 Multimeter" were used. With the K2400 currents of ± 10mA at room temperature and ± 1mA at low temperature were applied and with the K2000 the voltage drop in the coil was measured also using the four probe technique. Then the average of the absolute values of the two current directions was taken in order to avoid errors because of ther-

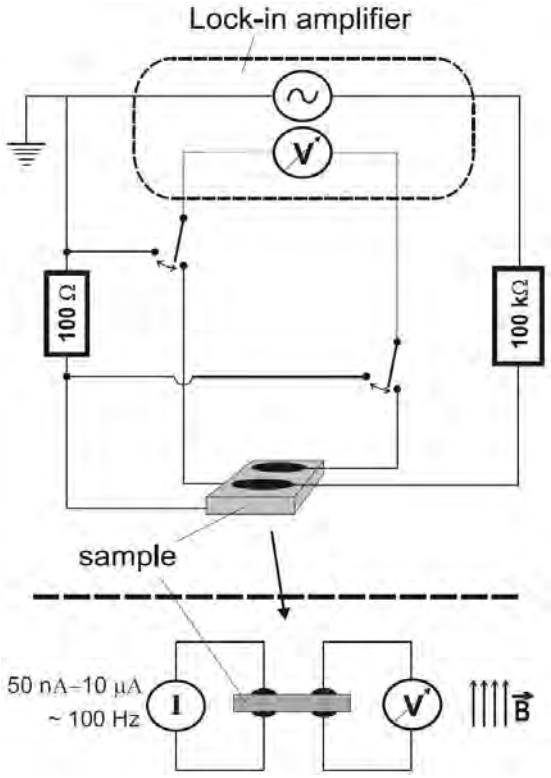

Figure 4.3: Circuit of the four point resistance measurement (taken from [15])

moelectric voltage. The process of changing current direction and averaging resistance was done by the computer.

4.2 Setup for the dilution fridge experiment

In this section the experimental setup for the dilution fridge experiment is presented. The setup consists of the pressure cell (clamp cell), which already was described in section 4.1.3, the dilution fridge insert, the vector magnet, the gas handling system and the measurement devices as well as the magnet power supplies. Devices were controlled and data was taken with the help of a LabView program written by Sebastian Jakob [16].

4.2.1 Dilution refrigerator

The dilution fridge insert used for this experiment already existed and can be seen in figures 4.4 (a) and (b). It contained a dilution unit originally built by K. Neumaier[1] and was assembled and wired by S. Jakob [16].

[1] Walther-Meißner-Institut

Dilution fridge unit

During its way through the dilution fridge unit the ^{3}He passes a spiral shaped heat exchanger (1) coupled with the helium bath, a Joule-Thomson heat exchanger (2) thermally coupled with the main pumping line, a heat exchanger coupled with the distillation chamber (3) and a counterflow heat exchanger (4), where concentrated ^{3}He flowing to the mixing chamber and the diluted ^{3}He flowing from the mixing chamber to the distillation chamber are thermally coupled. The impedances at (A) and (B) are needed to enable Joule-Thomson cooling. The tubes connecting the chambers (in order to make the insert stable) are made of Degussit[2] (C), which has a low heat conductivity.

The mixing chamber itself is filled with a labyrinth of sintered copper (D) at the bottom to increase thermal coupling between the mixture and the bottom of the mixing chamber. In the mixing chamber the barrier layer between concentrated and diluted phase of ^{3}He is located. When the diluted phase is pumped in the distillation chamber mainly ^{3}He evaporates because it has a higher vapor pressure than ^{4}He. That decreases the amount of ^{3}He in the distillation chamber resulting in a flow of ^{3}He from the mixing chamber into the distillation chamber. Now the diluted phase in the mixture lacks ^{3}He, which is replaced by ^{3}He from the concentrated phase. This dilution of ^{3}He costs energy and therefore the mixture as well as the mixing chamber is cooled down.

Mounting of the pressure cell and thermal coupling

The clamp cell was also used in the dilution fridge experiment. There PES (Polyethylensiloxan), which also is a silicon oil, was used as pressure medium instead of GKZh as our supply of GKZh was already rather old and already started polymerizing during the effective mass experiment. However, it is dubitable that PES is an adequate alternative to GKZh as it seems to loose more pressure during cooling and there are some hints that the pressure inside the cell might not be completely homogeneous.

As can be seen in figures 4.4 (a) the pressure cell is screwed to a ring (E) which is fixed to the mixing chamber via three rods all of which are made of copper because they also are the only heat links between the mixing chamber and the cell. The rods are armed with individually isolated pins where the wires from the top of the insert and the wires from the cell can be soldered. On the ring a NiCr heater (100 Ω) was added in addition to the Dale 100 resistor as the NiCr was supposed to have even lower temperature dependence of resistance than the Dale 100.

During the first test cooling of the dilution fridge the thermal coupling between the ring and the mixing chamber was bad: The ring could easily be heated to above 100 mK with the mixing chamber staying below 30 mK and even heating of the ring with 40 nW was sufficient to keep it above 100 mK. Therefore the cooling power of the dilution fridge could not be resolved. After the test measurement the rods, the ring and the plate, which is screwed to the mixing chamber, as well as the bottom of the mixing chamber were cleaned of oxidized copper as well as possible.

Furthermore, the old German silver screws were replaced by new ones made of copper. Additionally, as the new NiCr heater proved itself to be good, the old Dale 100 heater

[2]Degussit: sintered Al_2O_3 from Friatec AG, Mannheim

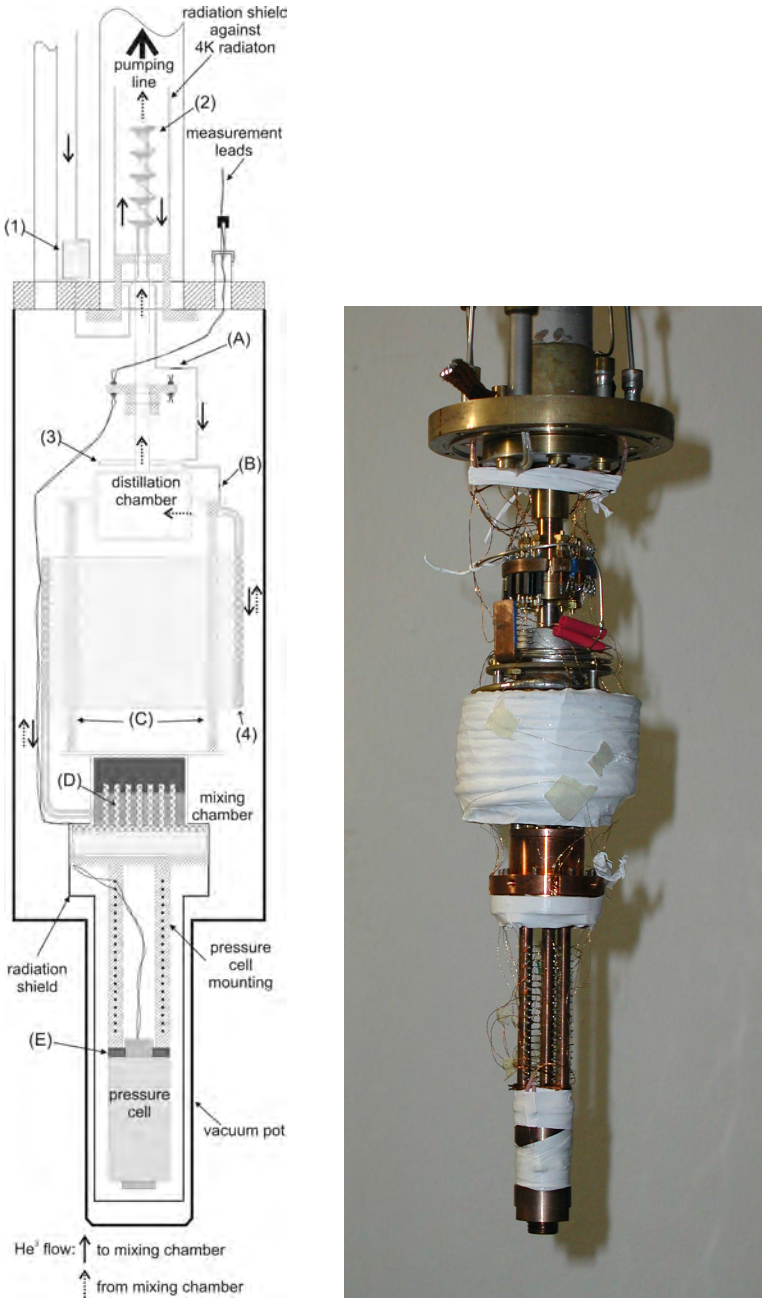

(a) (b)

Figure 4.4: (a) Schematical drawing and (b) photograph of the dilution fridge unit. Heat exchangers in the condensation line: (1) spiral shaped heat exchanger with the ^{4}He bath, (2) Joule-Thomson heat exchanger with the main pumping line, (3) heat exchanger with distillation chamber and (4) counter flow heat exchanger with the diluted ^{3}He. (A), (B) flow impedances, (C) Degussit tubes, (D) sintered copper, (E) copper ring (both taken from [16]).

was removed and its contacts were used for a second NiCr heater which was placed on the bottom side of the mixing chamber.

After these changes the thermal coupling between the ring and the mixing chamber was much better. When heating the ring to 100 mK the mixing chamber now showed a temperature of about 89 mK and when heating the mixing chamber to 100 mK the temperature of the ring stabilized at about 112.5 mK. The cooling power of the dilution fridge at $T_{\text{mixing chamber}} = 100\,\text{mK}$ could now be resolved to $P = 5.5\,\mu\text{W}$.

Gas handling system

As the dilution fridge lacked a gas handling system of its own, a new one was built during the first 5 months of the diploma work period by J. Geißmann[3]. It mainly consists of a control panel with valves regulating the gas flow. Attached to it are two tanks, where the ^{3}He can be stored. A vacuum pump is used for pumping the ^{3}He through the dilution fridge. To clean the ^{3}He gas from any impurities apart hydrogen, the gas handling system also includes a cold trap consisting of an activated carbon filter enclosed in liquid nitrogen. For the initial cooling of the dilution fridge, a compressor for applying gas pressures up to 3 bar was included.

4.2.2 Vector magnet

As we needed to apply magnetic fields in every given direction, a superconducting vector magnet[4] was used. It consists of a main coil (which is arranged vertical) with one additional correction coil at each end and a split coil arranged perpendicular to the main coil (horizontal). The vertical coil has an inner diameter of 38.5 mm and a field constant of $23.7\,\frac{\text{mT}}{\text{A}}$ and can be used for a field of up to 2 T (however we didn't risk to apply more than 1.8 T in our experiment). The horizontal coils field constant is $5.625\,\frac{\text{mT}}{\text{A}}$ and has a maximum field of 440 mT.

With these two coils the magnetic field can be applied at any given angle within the vertical plane determined by the axes of the two coils by adjusting the magnetic field strengths of the individual coils according to

$$\theta = \arctan\left(\frac{H_{\text{vertical}}}{H_{\text{horizontal}}}\right), \tag{4.1}$$

with a total field strength

$$H_{\text{total}} = \sqrt{H_{\text{vertical}}^2 + H_{\text{horizontal}}^2}. \tag{4.2}$$

Thereby an angular resolution of more than 0.001° can be reached.

The magnet is mounted on an insert of its own (shown in Figure 4.5). This magnet insert together with the cryostat can be rotated against the dilution fridge unit to alter the direction of the horizontal coil. This way the magnetic field can be applied in any given direction relative to the sample.

[3] Walther-Meißner-Institut

[4] Built at the Walther-Meißner-Institut by G. Eska

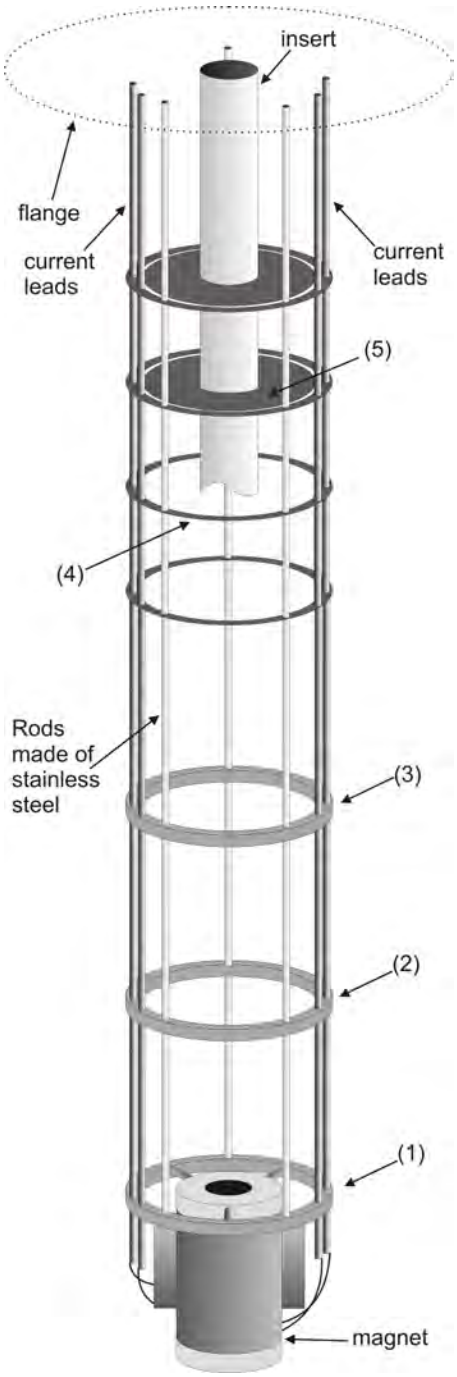

Figure 4.5: Mounting for the vector magnet. (1) - (3) rings for stabilization and carrying the magnet (4) radiation shields (5) radiation shields of the insert ("baffles"), (taken from [16])

However, there is a problem when using superconducting coils: There exist remanent magnetic fields adding to those applied by the magnets and shifting the angle of the total magnetic field. As the perpendicular critical fields of our samples are very low the perpendicular remanent field was measured every few measurements and compensated accordingly by applying an additional current to the vertical coil. The biggest vertical remanent fields measured during the low field ($\leq$ 330mT) measurements was 0.09 mT. After applying 1.8 T a remanent field of 3 mT was obtained. Therefore, the measurement at 1.8 T was done at the very end of the experiment. The remanent field of the horizontal coil could not be resolved because the samples are rather insensitive to weak parallel fields, which on the other hand made the effect of the horizontal remanent field negligible.

4.2.3 Definition of the angles for the magnetic field orientation

The definition of the angles describing how the magnetic field is oriented relative to the sample is given in Figure 4.6.

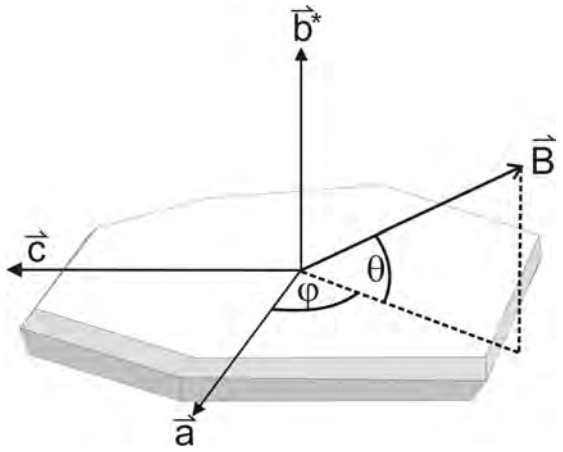

Figure 4.6: Definition of the angles used for describing the orientation of the magnetic field $\vec{B}$

The vectors $\vec{a}$, $\vec{b^*}$ and $\vec{c}$ stand for the crystal axes, where $\vec{b^*}$ is the axis perpendicular to the ac-plane. $\vec{B}$ represents the magnetic field. The orientation of the magnetic field relative to the *ac*-plane is given by the polar angle θ (with $\vec{B} \parallel ac-$plane at $\theta = 0$) and the azimuthal angle φ shows the orientation of $\vec{B}$ relative to crystal axis $\vec{a}$ (which is defined as $\varphi = 0$) within the *ac*-plane.

For the measurements two samples were mounted inside the pressure cell, contacted via platinum wires being their only support. The orientation of the samples had to be adjusted by hand and, thus, their alignments had an uncertainty of about $\pm 5°$. As α-(BEDT-TTF)$_2$KHg(SCN)$_4$ is very sensitive to small angular deviations of the magnetic field direction around the parallel orientation, only one sample at a time could be measured for such field directions. For that purpose the sample measured by S. Jakob at 2.8 kbar [16], hereafter referred to as sample #1, was chosen. Therefore the new

results could be compared with the former experiment. It also was the cleaner sample having a higher and sharper transition.

Another advantage of sample #1 was that it was already well characterized before, as it was used in several experiments including X-ray investigations. For that reason, the orientation of the crystal axes were known. The other sample, which is hereafter called sample #2, was never measured before, so the orientation of its crystal axes were unknown.

To obtain the correct value for the azimuthal angel φ, the initial orientation of the sample with respect to the horizontal coil had to be determined. Therefore the orientation of the sample was tracked to the top of the dilution fridge insert and marked on the top flange. The same was done for the horizontal field component. The error made in this process was estimated to about $\pm 5°$. The change of φ during the experiment was then traced by an angular scale fixed to the magnet and a tip fixed to the dilution fridge insert. With this method angular changes could be reproduced with an accuracy better than $\pm 0.5°$.

4.2.4 Measurement devices and magnet power supplies

Sample resistance

The sample and manganin resistances were measured the same way as in the effective mass experiment with the only difference that a PAR (Princeton Applied Research) 5210 lock-in amplifier was used for sample #2. This time the oscillator amplitudes were set to 0.5 V over a resistor of 10 MΩ resulting in a current of 50 nA. Compared to the effective mass measurement the current was chosen so small as otherwise the heating of the current would affect the sample temperature. The oscillator frequencies were set to 333 Hz (SRS 830) and 18 Hz (PAR 5210), respectively.

Thermometry

For measuring temperature Cernox and RuO_x resistive thermometers were used. The Cernox thermometer for measurements of temperatures above 1.4 K, the RuO_x for temperatures below 2K. The Cernox resistor with an ambient temperature (T=300 K) resistance of 60 Ω was attached to the cell. Also three RuO_x resistors were used: One attached to the side of the mixing chamber with an ambient temperature resistance of 2 kΩ, one on the ring ((E) in Figure 4.4) on the opposite side of the NiCr heater with an ambient temperature resistance of 800 Ω, both calibrated by K. Neumaier (WMI), and one attached to the cell, which also had an ambient temperature resistance of 800 Ω and was calibrated by D. Andres (WMI).

The thermometers were all measured using AVS 45 or AVS 46 resistance bridges that were read out by the computer via "Keithley 195A Multimeters" connected to the analog output of the resistance bridges. The temperature was controlled using a "Keithley 220 CurrentSource", applying a heating current calculated by the computer (see section 4.2.5) to one of the two 100 Ω NiCr heaters mentioned above. After some tests we came to the following conclusion: It is better to use the mixing chamber heater, when doing temperature sweeps as the measured hysteresis is much smaller than with

the ring heater. And that it is better to use the ring heater, when stabilizing a given temperature because with the mixing chamber heater it is hard to get exactly the desired temperature at the cell.

Magnet power supplies

In the beginning a "Heinzinger TNSU 6-60" with a maximum output current of 60 A was used for the horizontal coil and a power supply built by U. Guggenberger[5] delivering ±1 A was used for the vertical coil. Both power supplies were controlled by analog d.c. voltage generated by either "Hewlett Packard 3245A Universal source" or the auxiliary output of the PAR 5210 lock-in amplifier. For the AMRO measurement the Guggenberger power supply was replaced by an "Oxford IPS 120-10" with a maximum output current of ±120 A (the same model as used in the effective mass experiment).

At one time during the measurements the Heinzinger power supply broke down and was then replaced by the Oxford IPS 120-10 as controller of the horizontal field until the end of the angle dependent measurements. For the Shubnikov-de Haas oscillation measurement the Oxford power supply was used for the vertical field.

4.2.5 Software

To operate the devices a LabView program written by Sebastian Jakob [16] was used. It contains functions for acquiring data, controlling temperature and controlling magnetic field. Most parts of the program were used as they were, however two improvements of the temperature control program could be achieved.

1. The first improvement affects the program's behavior when getting close to the setpoint ("temperature to reach") in a temperature sweep (or more exactly when entering a user defined interval ("interval to start stabilizing temperature") around this setpoint). In Sebastian Jakob's version, when inside this interval, the program only cared about the difference between the averaged temperatures and the setpoint, completely ignoring the rate when calculating the modification for the heating power. This resulted in an increasing of the sweep rate even when the temperature was coming close to the setpoint. The system then entered a state with a damped temperature oscillation around the setpoint until the oscillation amplitude became so low that the temperature could be called stable.

This behavior was improved by including the averaged sweep rate in the calculation of the modification of the heating power also in the "stabilizing temperature" regime as long as the temperature difference to the set value is decreasing in order to slow down the sweeping rate even before the set temperature is reached. The set rate is thereby calculated from the difference of "average temperature 1" and the setpoint. While the temperature difference to the setpoint is increasing the program works as before. As can be seen in Figure 4.7 the desired temperature is stabilized much faster by this improvement.

For both curves a heating rate of 5 mK/min, a set temperature of 65 mK and identical time constant and weighting factors were used.

[5] Walther-Meißner-Institut

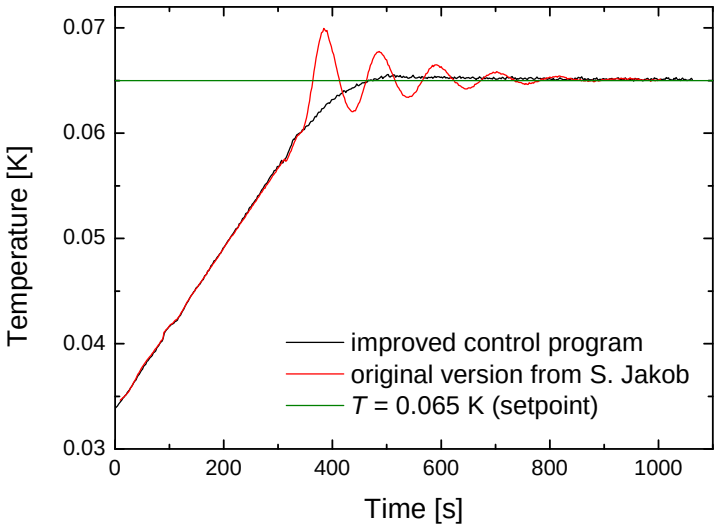

Figure 4.7: Time dependent behavior of temperature with the old and new versions of the program with heating rate of 5 mK/min and setpoint of 65 mK

The way the improved program is working in the "stabilizing temperature" regime can be illustrated with the following sequence:

- Determine whether the difference between "averaged temperature 1" and the "temperature to reach" is decreasing or increasing
- If it is decreasing:
  - Calculate the "rate to keep" from the difference between averaged and set temperature
  - Calculate the modification for the heating power the same way it would be calculated in the "keeping rate" regime, using the "rate to keep" calculated before
- If it is increasing:
  - Calculate the modification for heating power depending on the difference between averaged and set temperature (like it was before)
- From there the program continues as before

2. As the second improvement a possibility of ramping the set point was added to the temperature control program. If this option is used for a temperature sweep the setpoint is ramped, while otherwise the rate was stabilized. With this method one can make sure that the final temperature is reached in the calculated time in contrast to the method of just keeping the rate, where always time is lost, especially in the beginning.

On the other hand the development of the rate is smoother when stabilizing the rate, especially at the start of the sweep, where the rate always makes some oscillations in the ramping mode.

5 Results and discussion

In this chapter the experimentally acquired data are presented and the conclusions taken from them are discussed. Section 5.1 covers studies of the SdH oscillations in a ^{4}He cryostat at different pressures in order to evaluate the pressure dependence of the effective cyclotron mass of the charge carriers on the cylindrical Fermi surface sheets in α-(BEDT-TTF)$_2$KHg(SCN)$_4$.[1]

In section 5.2 preliminary measurements in the dilution fridge at ambient pressure are presented that were mainly done to charcterize the samples. This was especially important as sample #2 had never been measured before. In section 5.3 measurements under a pressure of $p = 3.4$ kbar are discussed. In those measurements the dependence of the superconductivity on different magnetic field angles was investigated in detail.

During all measurements the measured value was the interplane resistance of the samples.

5.1 Pressure dependence of the effective cyclotron mass

α-(BEDT-TTF)$_2$KHg(SCN)$_4$ undergoes a phase transition from a charge-density wave (CDW) state to a normal metallic state at increasing pressure (see Fig. 3.6), crossing a quantum critical point (QCP). Because many-body interactions are enhanced there, such QCPs tend to go along with anomalies in the pressure dependence of the effective cyclotron mass of the conducting electrons. Typically the effective cyclotron mass is known to decrease in organic metals when applying pressure. However, an unusual behavior of the effective cyclotron mass in the organic metal κ-(BETS)$_2$Mn[N(CN)$_2$]$_3$ has already been reported recently by Zverev et al. [65]. So the intention of this experiment was to trace the evolution of the effective cylotron mass upon crossing the QCP. The cyclotron mass was determined by analysing Shubnikov-de Haas (SdH) oscillations.

As described in section 4.1 these measurements were done in a ^{4}He-cryostat containing a 15 T superconducting solenoid. The magnetic field was applied perpendicular to the conducting layers.

To obtain the value of the effective cyclotron mass at a certain pressure $m_c(p)$ several magnetic field sweeps were done at different constant temperatures. In Fig. 5.1 some examples at ambient pressure are shown. The behavior of the magnetoresistance is typical for α-(BEDT-TTF)$_2$KHg(SCN)$_4$ at ambient pressure as already observed by Osada in 1990 [66]: First the resistance increases to a maximum at around 12 T and

[1] These measurements are performed together with Prof. V. N. Zverev, Institute of Solid State Physics, Russian Academy of Sciences, Chernogolovka, Moscow region 142432, Russia

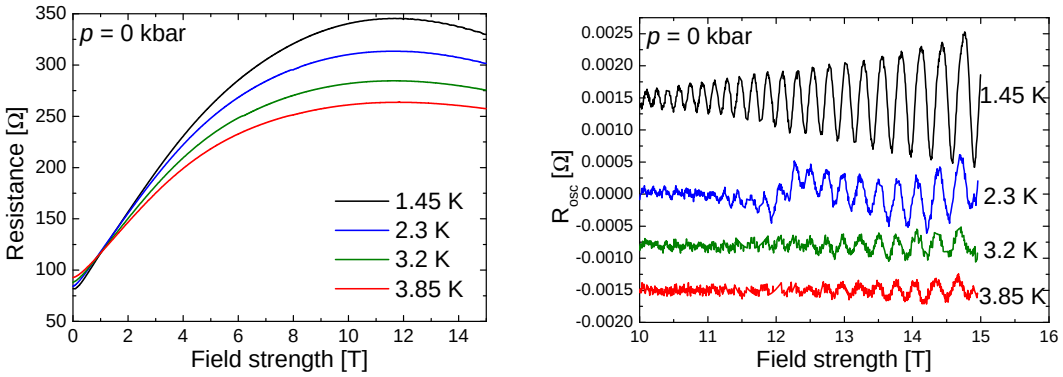

(a) (b)

Figure 5.1: (a) Magnetoresistance at different temperatures ($p = 0$ kbar). (b) SdH oscillations after subtracting the background resistance. The curves are vertically offset with respect to each other.

then starts going down again, eventually reaching a minimum at about 24T, which, of course, could not be reached with our 15 T magnet.

Even though the SdH oscillations are always rather small in this compound at ambient pressure for $B \leq 15$ T, for the current sample they seem to be even smaller than average. This is due to the fact that we have chosen a relatively low-quality sample to make sure that even at high pressure we get no considerable second harmonic or beating. This was done because high-quality samples have a anomalously strong high-harmonic content, even at $B = 15$ T [66–69]. Therefore it is difficult to analyse the SdH oscillations because such effects violate the Lifshitz-Kosevich theory (section 2.3.1) and the FFT (fast-fourier-transformation) spectrum becomes complicated. In a low-quality sample

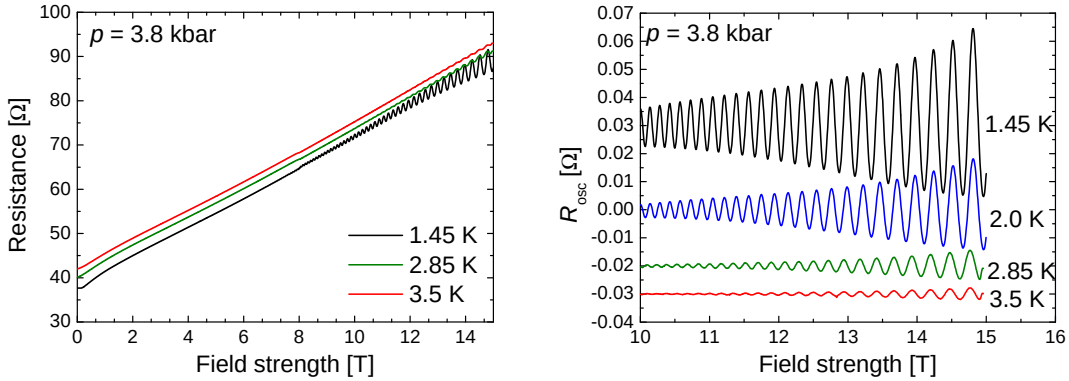

(a) (b)

Figure 5.2: (a) Magnetoresistance at different temperatures at $p = 3.8$ kbar. (b) SdH oscillations after subtracting the background resistance. The curves are vertically offset with respect to each other.

only the first harmonic is dominant resulting in simple FFT spectra, which are easy to analyse to obtain m_c.

At high pressures we observe an altered behavior of the magnetoresistance and an increase in the oscillation amplitude as shown in Fig. 5.2. The field dependence of the magnetoresistance still shows some very small bendings indicating that even at this pressure of $p = 3.8\,\mathrm{kbar} > p_c \approx 2.5$ kbar we still are entering the field induced charge density wave (FICDW) state (described in section 3.4.2). The relative oscillation amplitude at this pressure is increased by a factor of ~ 100, as compared to the ambient pressure case. The absolute amplitude increases by a factor of ~ 30, while the background resistance decreases by a factor of ~ 3.5. The oscillation amplitude starts decreasing again at 6 kbar.

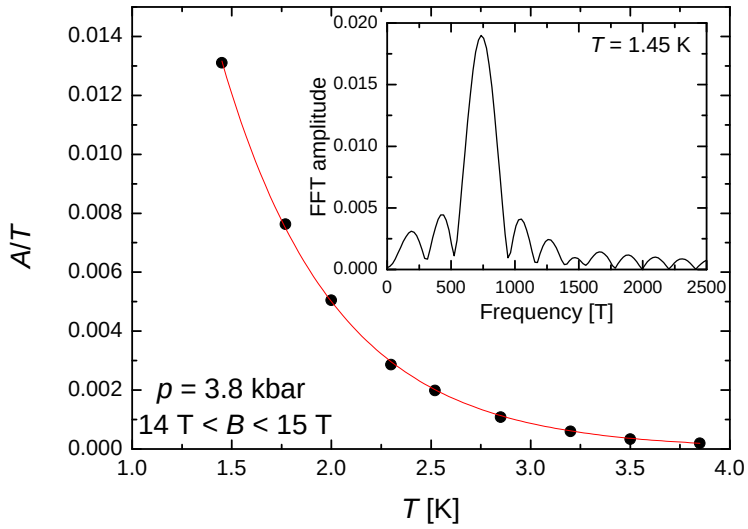

Figure 5.3: FFT amplitude of the SdH oscillations A divided by temperature T plotted as a function of T. The points were taken in a field window of $14\,\mathrm{T} < B < 15\,\mathrm{T}$, at $p = 3.8$ kbar. The red line represents a fit using the LK theory [39]. The inset shows the FFT spectrum of the $T = 1.45$ K field sweep in the same field window.

When looking at the data taken at many different pressures (which are not shown here), we can see that the bending features start showing up at about 1.5 kbar. The overall $R(B)$ behavior of the background turns linear when the critical pressure of 2.5 kbar is exceeded, but the bendings still are visible there. They are, however, unreliable as an indicator for the phase boundary of the FICDW state, because they weaken very smoothly with increasing pressure. Since the bendings are already hardly visible in the $p = 3.8$ curves it is, therefore, impossible to tell at which pressure this feature completely vanishes.

To evaluate the effective cyclotron mass m_c, first FFT spectra of the oscillatory part were made in a fixed field window. An example of such a FFT spectrum at $p = 3.8$ kbar and $T = 1.45$ K for a field window of $14\,\mathrm{T} < B < 15\,\mathrm{T}$ is shown in the inset of Fig.

5.3. Then the obtained FFT amplitude was divided by temperature and plotted versus temperature, as shown in Fig. 5.3. After that it was fitted with the formula for the LK temperature damping factor (equation 2.25). From the fit we thus obtain a value for the effective cyclotron mass in units of the free electron mass $m^* = m_c/m_e$.

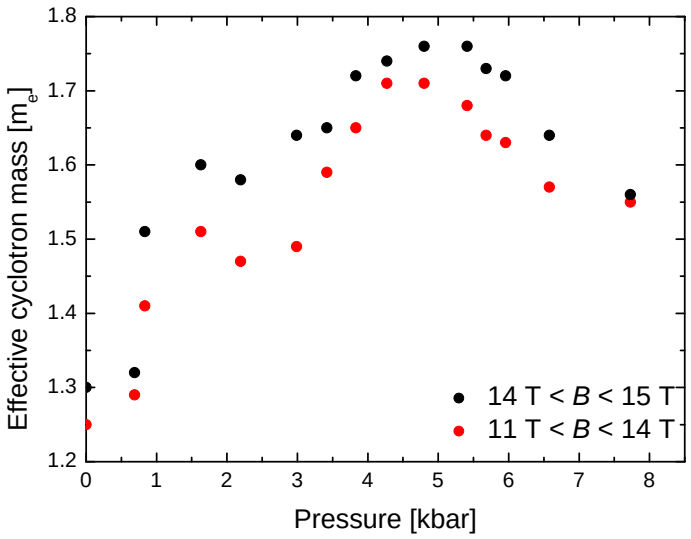

Figure 5.4: Pressure dependence of the effective cyclotron mass in units of the free electron mass.

This procedure was done for all pressures in two different field windows 11 T $< B <$ 14 T and 14 T $< B <$ 15 T resulting in the dependence shown in Fig. 5.4. For the ambient pressure, at which our compound is in the CDW_0 state with a fully gapped q1D part of the FS, literature data on m^* give values in the range 1.2-1.6 [15, 67–71]. Our values lie in the lower part of this range and is therefore reasonable. We can see that the effective mass increases with pressure until it reaches a maximum at $p \approx 5$ kbar and then starts decreasing again. As there are not very many points at each pressure and also some scattering in the obtained FFT amplitudes (the lowest temperature point for example was deemed unreliable at many pressures) the error of m^* has to be estimated to at least ± 0.05, so not more than the general behavior of the effective mass can be read from this measurement.

This behavior of the effective cyclotron mass is rather unusual, because, as mentioned above, m_c normally tends to decrease with increasing pressure. Such an unusual behavior was, however, expected for our compound, because of enhanced many-body interactions near the transition from the CDW to the normal metallic state. For the case of a low magnetic field the peak would have been suspected to be at $p \approx 2.5$ kbar. But as we have rather high fields the shift of this maximum to $p \approx 5$ kbar could be due to the field induced CDW state, which is known to exist at $B \approx 10$ T at $p > p_c$ [13], with the maximum pressure remaining unknown yet. Also the rather big difference between

the results from the two field windows at pressures of 2-3 kbar may originate from the fact that at these pressures the transition from the CDW_0 to the FICDW state occurs at $B \approx 14$ T. So it could be that the maximum of m^* marks the critical pressure, at which even the FICDW state is suppressed. To verify this explanation, however, further measurements are required.

In order to find the transition from the CDW_0 to the normal metallic state experiments at a lower field and higher temperature range are necessary to rule out an influence of the FICDW state.

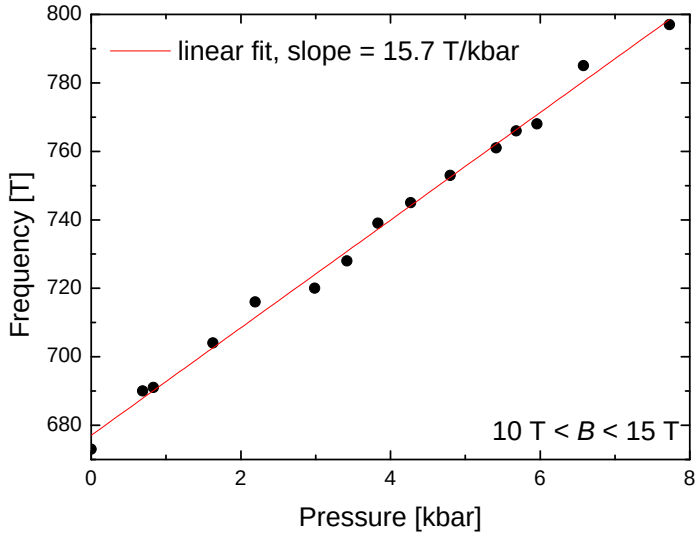

Figure 5.5: Pressure dependence of the oscillation frequency.

From this set of experiments also a pressure dependence of the oscillation frequency could be extracted, shown in Fig. 5.5. Therefore the largest possible field window of $10\,\mathrm{T} < B < 15$ T was used in order to reduce the error. The slope of 15.7 T/kbar is somewhat lower than the 16.7 T/kbar measured by D. Andres [15] earlier. The difference, however, lies within the uncertainty of the pressure determination.

5.2 Dilution fridge measurements at ambient pressure

5.2.1 Sample characterization

A first good indicator for the sample purity is its resistive behavior from room temperature down to 4 K, shown in Fig. 5.6. As we can see, both samples show metallic character at low temperatures, however, while the resistance of sample #1 is more or less constant down to 100 K and then drops with a steep slope, sample #2's resistance grows down to 250 K and then drops down with a much slower rate. A steeper slope of $R(T)$ at low T is a sign of a higher sample quality.

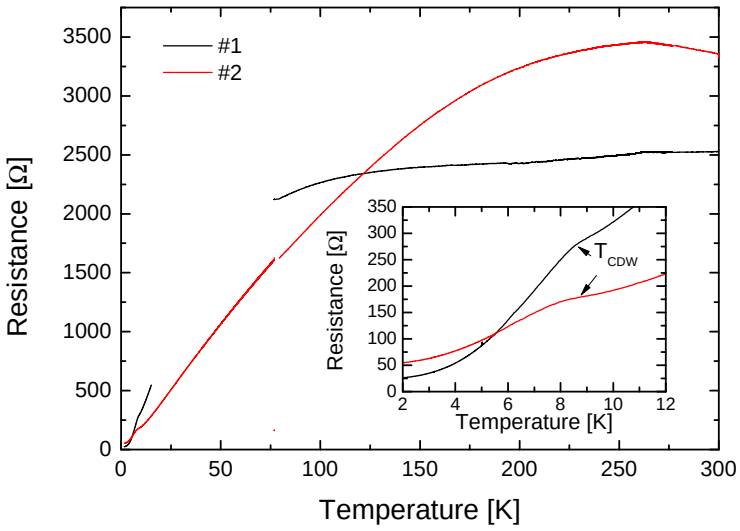

Figure 5.6: Temperature dependence of the resistance (the missing data in the curve for sample #1 follows from too late switching of the lock-in amplifier sensitivity). The inset shows the anomaly (hump) at 8.5 K caused by the transition into the CDW state.

Another possibility to estimate sample purity is the residual resistance ratio (RRR) i.e. the ratio of the resistance at room temperature and at low temperature. For sample #1 we have:

$$\frac{R(300\,\mathrm{K})}{R(1.6\,\mathrm{K})} = \frac{2600\,\Omega}{25\,\Omega} = 104 \tag{5.1}$$

and for sample #2:

$$\frac{R(300\,\mathrm{K})}{R(1.6\,\mathrm{K})} = \frac{3200\,\Omega}{50\,\Omega} = 64 \tag{5.2}$$

So both the slope and the RRR suggest that sample #1 is cleaner, therefore it was the sample of choice for all measurements, which could not be done for both samples at once. The RRR of sample #1, however, is smaller than the one measured by S. Jakob for the same sample at ambient pressure [16]. He measured the same resistance

value for low temperature but the room temperature value $R(300\,\mathrm{K}) = 3000\Omega$ was considerably higher. This difference might either be caused by aging of the sample or some small amount of the graphite paste used for gluing the contact wires on the sample (see section 4.1.4) may have flowed over the edge of the sample covering some part of the sides and thereby shortening some of the layers. In the latter case the room temperature value would drop while the low temperature value would stay the same as in the low temperature range the effect of the graphite can be neglected due to the much higher sample conductivity.

The inset of Fig. 5.6 shows the hump in the resistance of both samples at 8.5 K indicating the transition to the charge density wave (CDW) state.

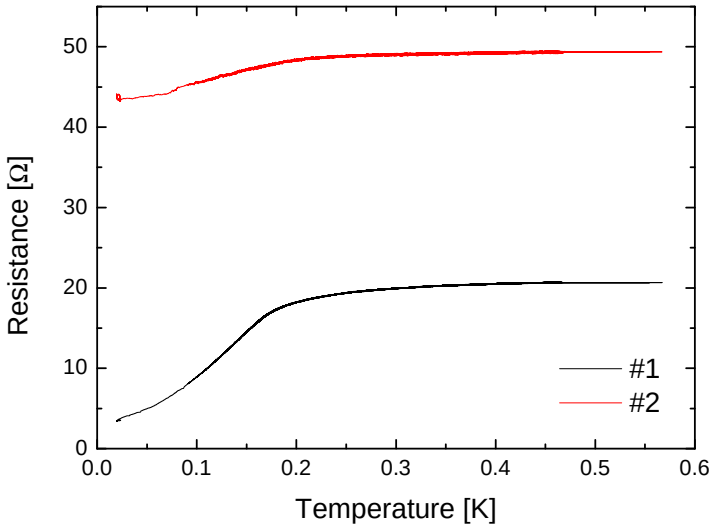

Figure 5.7: Low temperature part of the $R(T)$ dependence featuring the partial superconducting transition

Fig. 5.7 displays the resistive behavior of the samples at temperatures down to 20 mK. Below 200 mK we can see a broad superconducting transition in both samples, with, however, a much smaller resistance drop in sample #2. The resistance doesn't drop to zero as the CDW prevents the sample from becoming completely superconducting. Instead a mixed state of CDW and filamentary superconductivity is formed. The competition between CDW and superconductivity was investigated in detail by D. Andres et al. [7, 14, 15].

We also checked the dependence of $R(T)$ on the measuring current applied to sample #1 at very low temperatures, see Fig. 5.8. Seemingly a current of 100 nA is too high as the resistance is increased by more than 50% compared to 50 nA and 20 nA where the difference is not very big anymore. The 20 and 50 nA curves are shifted vertically not horizontally. Therefore this shift is not due to overheating but rather an effect of the filamentary superconductivity (see [7]). As the noise at 20 nA already grows pretty

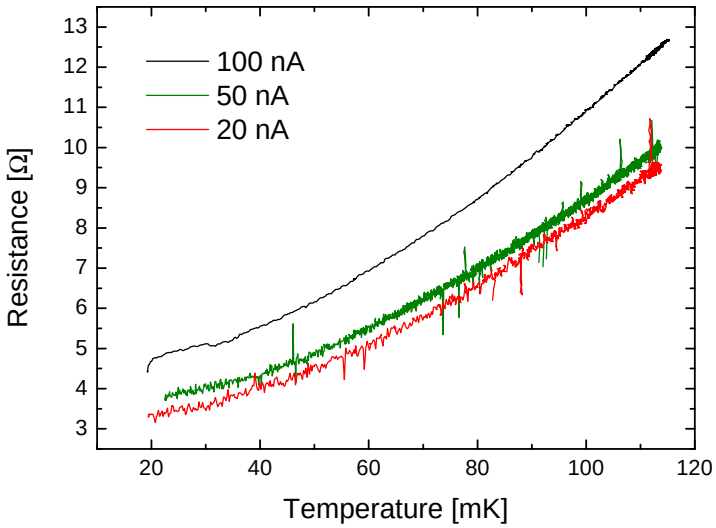

Figure 5.8: Temperature sweeps with different measuring currents

strong we decided to stay at 50 nA for further measurements.

When applying a magnetic field in different directions relative to the conducting layers one immediately sees the anisotropic behavior of α-(BEDT-TTF)$_2$KHg(SCN)$_4$.

For a field in the direction perpendicular to the conducting layers, shown in Fig. 5.9 (a), the superconductivity breaks down very quickly. At a temperature of 100 mK the superconducting state is destroyed completely at about 8 mT. For the same temperature, a field applied parallel to the layers destroys the superconductivity much

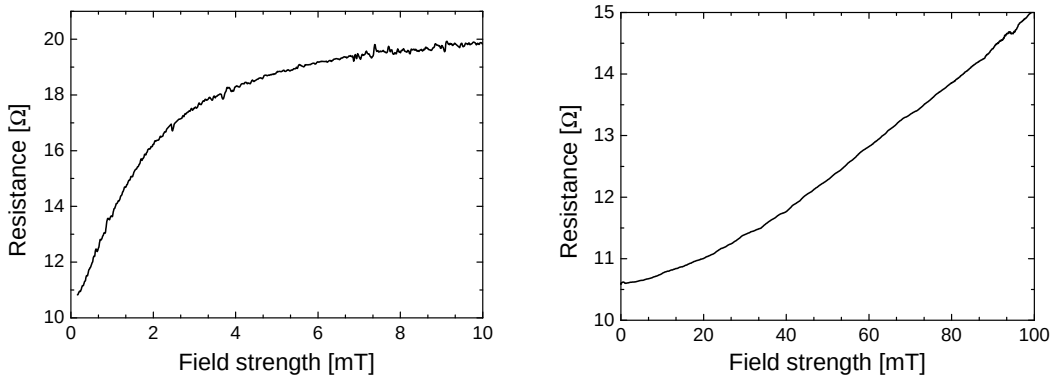

(a) (b)

Figure 5.9: Field dependence of resistivity for magnetic field (a) perpendicular and (b) parallel to the conducting planes at 100 mK.

slower and even at 100 mT the resistivity of the sample still has not reached the normal state value.

5.2.2 Angle-dependent magnetoresistance oscillations

The best way to check the azimuthal orientation of the sample (the φ-angle) is measuring angle-dependent magnetoresistance oscillations (AMROs). An example of AMROs at different φ-angles is given in Fig. 5.10. As we can see, the AMROs for the magnetic field direction parallel to the c-axis are more pronounced and have a higher period than for a field parallel to the a-axis. Considering the theoretical estimations (presented in section 3.4) the AMRO amplitude and period should be largest for a magnetic field in the direction parallel to the nesting vector $\vec{Q}$ (which is also parallel to the projection of the b-axis in the ac-plane) and the AMROs should completely vanish for a magnetic field perpendicular to $\vec{Q}$. When plotting the AMRO period versus the azimuthal angle φ, this dependence should have a minimum for the $\vec{B}$-rotation plane $\parallel \vec{Q}$ and diverge for the $\vec{B}$-rotation plane $\perp \vec{Q}$.

The AMRO period Δ is obtained by a linear fit of the value $\tan(90° - \theta_p)$ plotted against the order number p for each φ, where θ_p is the position of the pth order AMRO minimum (in comparison to Eq. 2.34 we have $90°-\theta$ because the θ is defined different). For most φ-angles only the position of the first order dips were used, as only they could be determined reliably. The φ-dependence of the AMRO period $\Delta(\varphi)$ is shown in Fig. 5.11.

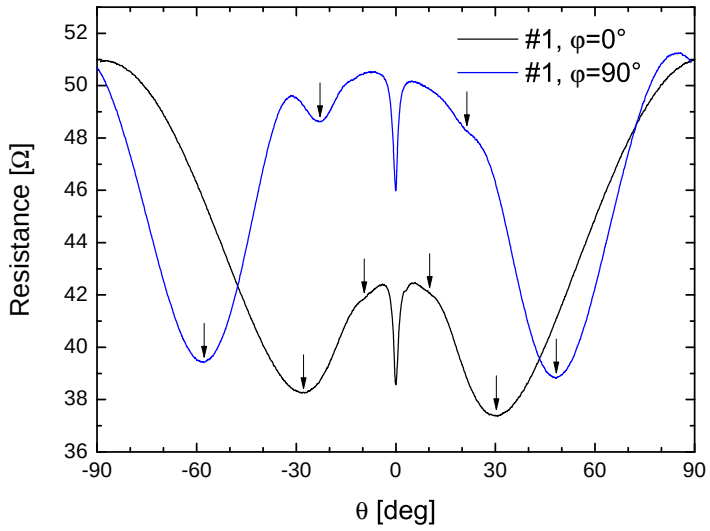

Figure 5.10: Example of angle-dependent magnetoresistance for sample #1 featuring AMROs. $\varphi = 0°$ is parallel to a-axis and $\varphi = 90°$ is parallel to c-axis, $T = 100$ mK, $\mu_0 H = 300$ mT. The arrows point to the dips of the AMROs originating from the LMA effect.

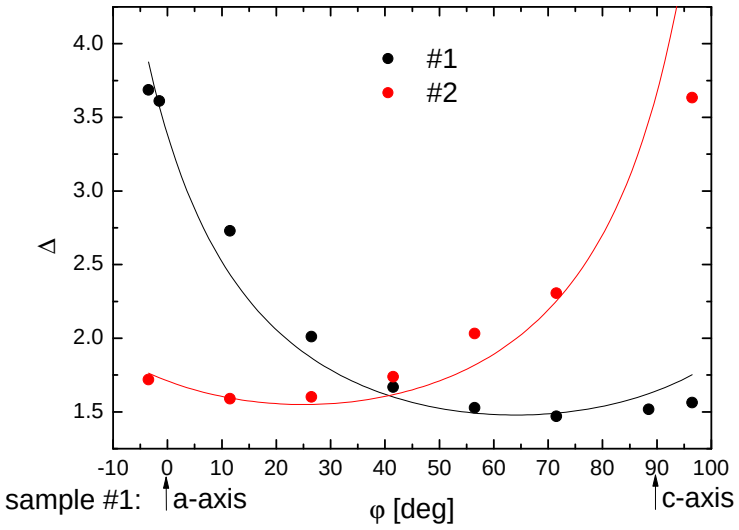

Figure 5.11: φ-dependence of the AMRO period Δ. $\varphi = 0$ for the B-rotation plane $\parallel$ a-axis of sample #1. For sample #2 φ is arbitrary.

According to Kovalev et al. [72] this dependence can be fitted by the relation

$$\Delta(\varphi) = \frac{\Delta_0}{\cos(\varphi - \varphi_0)}, \tag{5.3}$$

where Δ_0 and φ_0 both are fitting parameters. The values of $\Delta_0 = 1.48$ for sample #1 and $\Delta_0 = 1.6$ for sample #2 we obtain are much bigger than the value evaluated by Kovalev ($\Delta_0 = 1.25$), but our measurement has a rather big error bar because the AMRO features are not very strong, so maybe it is not very reliable. Another possible explanation is that we are at very weak fields so $\omega_c\tau < 1$. The theory of Kovalev, however, is only valid for the case of strong magnetic fields ($\omega_c\tau \gg 1$) so the AMRO positions may be shifted. But the direction of $\vec{Q}$ (and also the parameter φ_0) should be the same. So the estimation for the direction of the axes we obtain should be reliable.

Figure 5.11 confirms that for sample #1 we have a minimum of Δ at an angle of 20°-30° relative to the c-axis, as suggested in earlier measurements, however, determining the exact position of the minimum is rather difficult because of its broadness. Unfortunately the angle where Δ diverges is not resolved in the measured interval of φ. From this measurement we can derive at least that known directions for the crystal axes in sample #1 seem to be correct and make an estimation of how they are oriented in sample #2.

5.2.3 Azimuthal angle anisotropy at ambient pressure

The former measurements by S. Jakob [16] have shown a considerable anisotropy of the critical field parallel to the layers at $p = 2.8$ kbar. For an understanding of this anisotropy it is of interest to look for inplane anisotropy at ambient pressure, too.

The anisotropy of α-(BEDT-TTF)$_2$KHg(SCN)$_4$ for parallel magnetic fields applied at different azimuthal angles φ was examined by doing θ-sweeps in a range of $\sim \pm 7°$ around the orientation parallel to the planes at different φ-angles. Some example curves are given in Fig. 5.12. This experiment was done in steps of $\varphi = 20°$ over a angular range of 180°.

The anisotropy of the normal state magnetoresistance (R_{ns}) was obtained by taking the resistance value at the point where $\theta = 5.5°$, and is shown in Fig. 5.13 (a) as a function of φ (black circles). The empty circles represent the same data as the filled out ones, but are shifted by 180° to get a clearer view of whole angular range. This procedure is valid, because the anisotropy does not depend on the "sign" of the magnetic field. As the angular sweep curves look very similar this estimation for the normal state magnetoresistance is qualitatively correct and should only differ by a constant factor from the normal state magnetoresistance at an exactly parallel field.

The resistance in the dip, presented in Fig. 5.13 (a) (red circles), has almost the same angular dependence as the normal state magnetoresistance and shows a maximum between $\varphi = 40°$ and 50°. To obtain the anisotropy of the superconducting state the difference of the above measured normal state magnetoresistance and the resistance at exactly the parallel field direction (the minimum values at the dips as seen in Fig. 5.12) was taken. Thus we get some indicator of the "strength" of the superconductivity in the form of the resistance drop between the normal state and the superconducting state. The value of the resistance drop normalised to the normal state magnetoresistance for fields in this direction is shown in Fig. 5.13 (b). There we can clearly see that the superconductivity is strongest at around $\varphi = 60°$. The anisotropy of the normalised

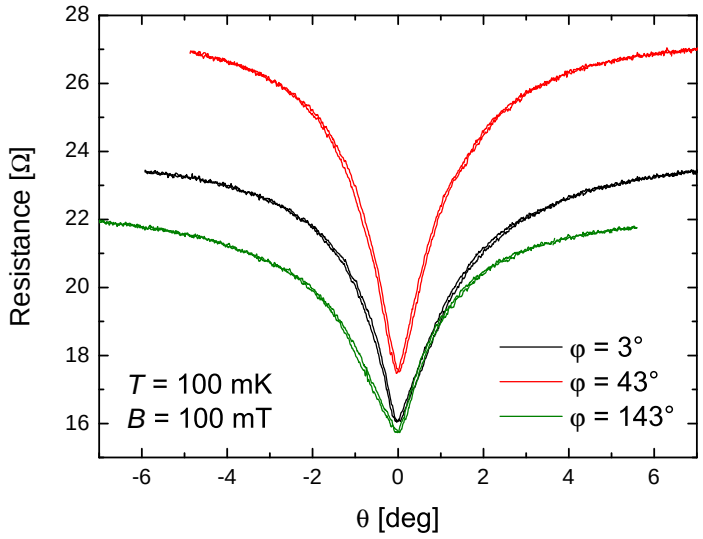

Figure 5.12: Angular sweeps (up and down) of the magnetic field around θ with different φ with a field of 100 mT at 100 mK.

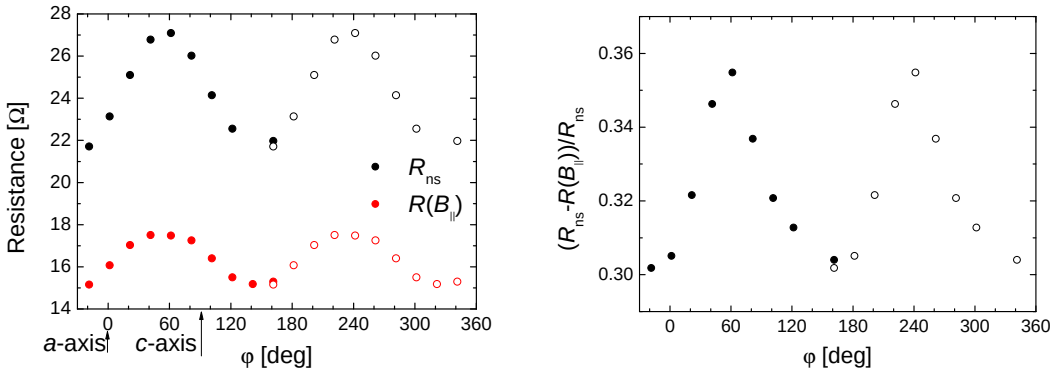

(a) (b)

Figure 5.13: (a) φ-dependence of the normal state magnetoresistance (R_{ns}) and the resistanc in the dips $R(B_{\|})$. (b) φ-dependence of the resistance drop due to superconductivity normalised to R_{ns}. The empty circles represent the same data, as the filled out ones shifted by 180°.

resistance drop amounts to almost 20%.

In Fig. 5.14 the normal state magnetoresistance is displayed in the form of a polar plot together with the cylindrical part of the FS. As we see, the anisotropy of R_{ns} does not quite coincide with the shape of the cylindrical FS cross section, but is shifted by some 30°. According to theoretical estimations by Lebed and Bagmet [73] we would expect the maximum of the normal state magnetoresistance to coincide with the max-

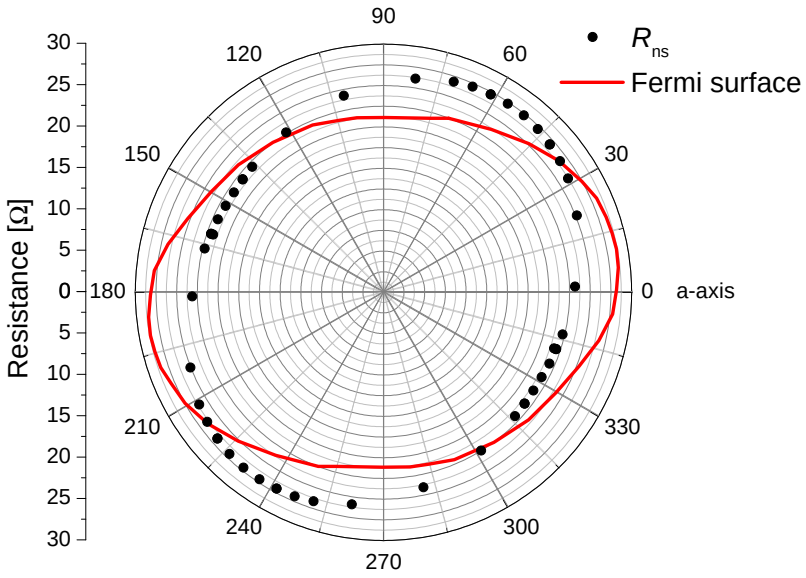

Figure 5.14: Polar plot of the normal state magnetoresistance (R_{ns}) and the cylindrical Fermi surface sheet of α-(BEDT-TTF)$_2$KHg(SCN)$_4$ calculated by Kovalev et al. [72].

imum of the FS. This obviously is not the case in our measurements, so we cannot understand at present, which effect is responsible for the φ-dependence of the normal state magnetoresistance.

5.3 Dilution fridge measurements at $p = 3.4$ kbar

After finishing the ambient pressure measurements the clamp cell containing the samples was pressurized at room temperature. We planned to perform the experiments at a pressure approximately 0.5 kbar above the value of the former experiment by S. Jakob at $p \approx 2.8$ kbar [16]. Knowing that there is a considerable drop of pressure on cooling we applied 6.5 kbar at room temperature. To determine the pressure at low temperatures we had several possibilities: At $T \approx 15$ K the manganin resistance was measured as mentioned in section 4.1.4. The obtained value was compared to the value measured at the same temperature at ambient pressure. Also the SdH oscillation frequency obtained from the high field measurement, which is described in section 5.3.1, was analysed and compared with the pressure dependence obtained during the effective mass experiment (Fig. 5.5). Based on both methods the low temperature pressure was estimated to 3.4 ± 0.1 kbar. Thus we were very near the intended value.

5.3.1 Characterization measurements under pressure

SdH oscillations

At the end of the pressure experiment measurements of SdH oscillations were performed with these two samples, both in the dilution fridge, at temperatures of 50-250 mK and perpendicular fields up to 1.8 T, and in the ^{4}He magnet cryostat at temperatures of 1.4-4 K and fields of up to 15 T. The effective cyclotron mass and the oscillation frequency under the given pressure are both good indicators for the applied pressure and the Dingle factor allows estimations of the purity of the samples.

The resistive behavior of both samples over the full field range is shown in Fig. 5.15. The superconducting transition, which at the lowest temperature takes place below 4 mT is not resolved in this plot. The insets show magnifications of both curves at around 1.7 T, where we can see oscillations of sample #2 with an amplitude of about 0.6% of the background resistance while for sample #1 the oscillation amplitude lies below the noise level of 0.4% of the background resistance and therefore can not be resolved.

The SdH oscillations of sample #2 were measured at different temperatures, some of which are shown in Fig. 5.16, in order to determine the effective cyclotron mass, which was calculated the same way as in section 5.1. The obtained value in the field range of 1.7-1.8 T was

$$m_c = 1.72\, m_e. \tag{5.4}$$

In Fig. 5.15 it is also noteworthy that both curves have a negative curvature until the highest shown field of 1.8 T. This is a signature of the normal metallic state in this material [74]. In the earlier experiments at 2.8 kbar [16] the resistivity of sample #1 already started bending upwards again at 1.7 T due to a transition to the FICDW state.

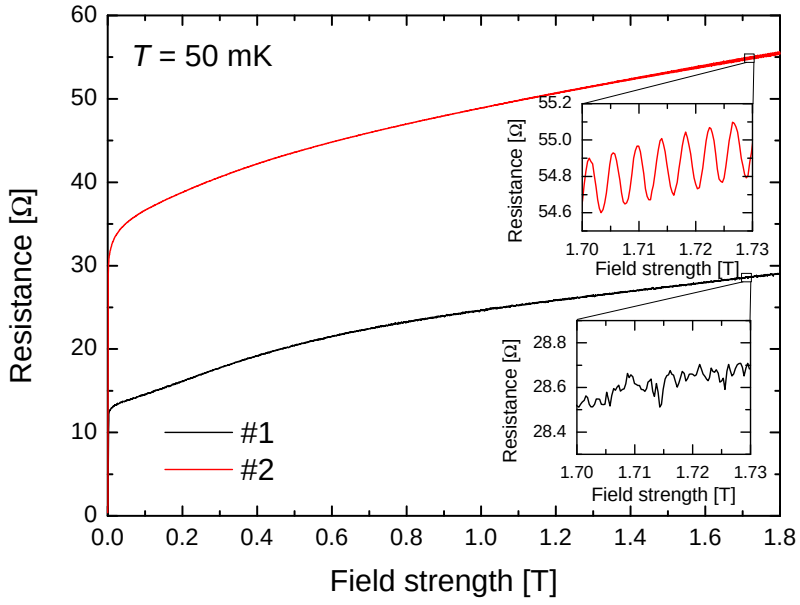

Figure 5.15: Dependence of the resistance of magnetic field perpendicular to the layers for both samples at 50 mK. In the insets we see that while sample #2 shows nice oscillations, those of sample #1 can not be resolved over the noise.

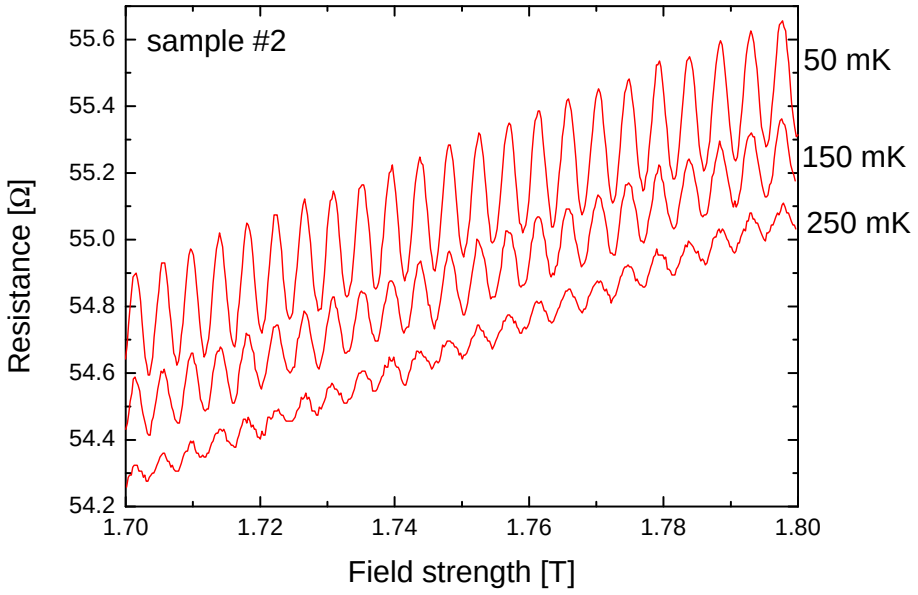

Figure 5.16: SdH oscillations of sample #2 at different temperatures.

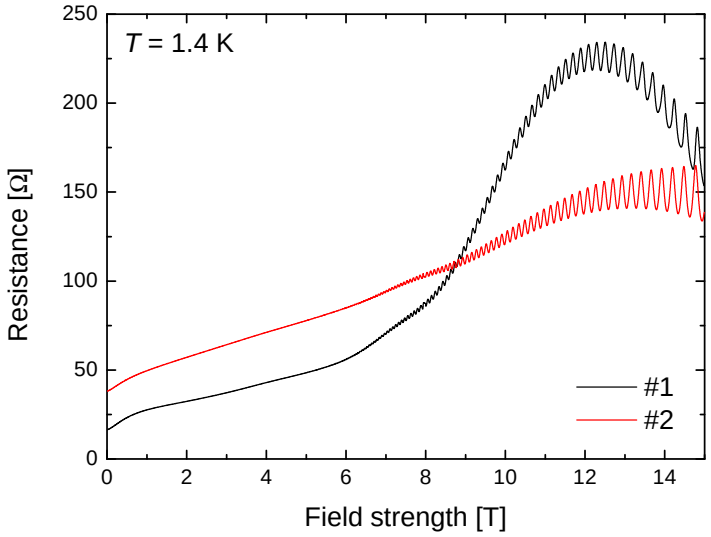

Figure 5.17: Field dependence of resistance up to 15 T at 1.4 K.

Furthermore, after finishing the dilution fridge experiment, the pressure cell was inserted into the ^{4}He cryostat with a 15 T magnet without changing the pressure to measure also the high field SdH oscillations of both samples. The resulting curves for the lowest possible temperature of 1.4 K are shown in Fig. 5.17. Starting at 6 T sample #1 shows a pronounced increase of resistance associated with the entrance in the FICDW state. For sample #2 this feature is far less pronounced, which indicates once more that sample #1 is cleaner. On increasing the temperature these anomalies due to the FICDW state become weaker as reported by D. Andres [13]. The values of the effective cyclotron mass obtained from the high field measurement are $m_c = 1.66\, m_e$ for sample #1 and $m_c = 1.71\, m_e$ for sample #2. This value of m_c for sample #2, therefore, is in excellent agreement with the value obtained at low temperatures.

Temperature dependence of resistance

Under pressure the shape of the temperature dependence of resistivity between 300 K and 2 K, shown in Fig. 5.18, has changed compared to the measurement at ambient pressure (Fig. 5.6). The resistance is lower over the whole temperature range, because the higher pressure results in an increased overlap of the electron orbitals of different layers and, therefore, an enhanced interlayer transfer integral.

The curvature changes at about 15 K. At lower T the resistance starts to saturate until the superconducting transition is reached (not shown in Fig. 5.18). But even near the transition there still is a small T-dependence of resistance. No hump indicating the CDW state is seen anymore. This proves that we are above the critical pressure for the CDW_0 state $p_c \approx 2.5$ kbar and, therefore, in the purely metallic state. From these measurements we can again calculate the residual resistance ratios for both samples,

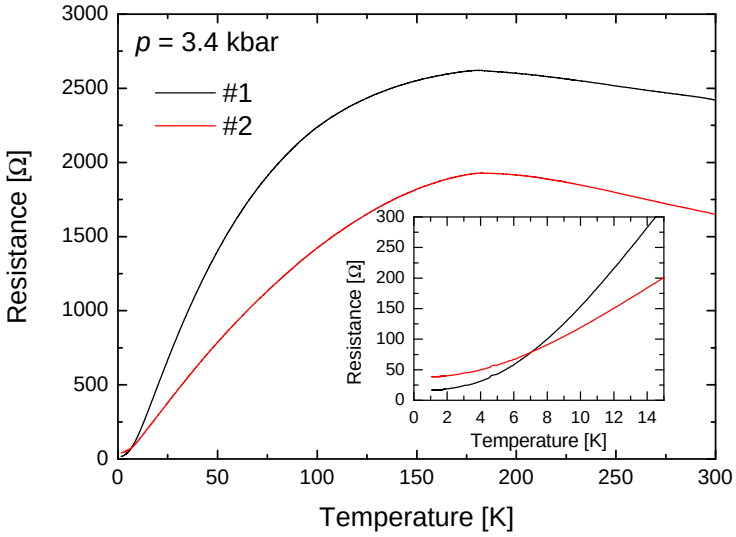

Figure 5.18: Temperature dependence of the sample resistance under pressure. The inset shows the low temperature part in which no anomaly can be detected any more. This indicates that the CDW state is suppressed.

obtaining

$$\frac{R(300\,\mathrm{K})}{R(1.6\,\mathrm{K})} = \frac{2320\,\Omega}{17\,\Omega} \approx 136 \tag{5.5}$$

for sample #1 and

$$\frac{R(300\,\mathrm{K})}{R(1.6\,\mathrm{K})} = \frac{1600\,\Omega}{40\,\Omega} = 40 \tag{5.6}$$

for sample #2. So, for sample #1 the ratio has increased compared to ambient pressure, what rather confirms the above mentioned assumption that some part of the samples edge was covered by graphite paste during contacting (described in section 5.2.1), as the effect of the paste also decreases on pressurizing.

Superconductivity

When cooling further a superconducting transition begins at about 104 mK as can be seen in Fig. 5.19. The transition width ΔT_c defined as the temperature range between 10% and 90 % of the normal state resistance R_{ns} measures about 12 mK for sample #1, being somewhat larger than the value registered by S. Jakob [16] (as shown in the inset of Fig. 5.19). This may be due to the effect of pressure inhomogenity in the PES. On the other hand, one cannot exclude some effect of aging of the sample. The critical temperature value obtained by the construction discussed below is 100 mK, which is in very good agreement with former measurements under pressure [7].

The transition of sample #2 is more complicated as it first shows a flatter slope in the range where the resistance is above 70% of R_{ns}, which is followed by a steep slope until

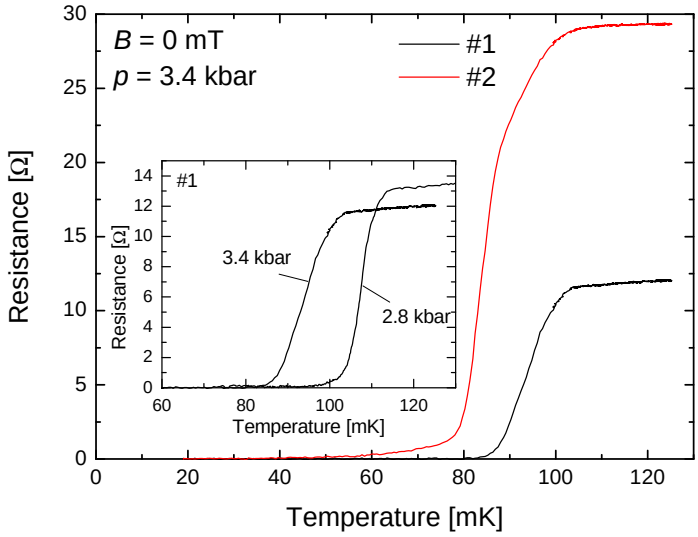

Figure 5.19: Superconducting transition of α-(BEDT-TTF)$_2$KHg(SCN)$_4$ without field. The inset shows the comparison of the transition of sample #1 at 2.8 kbar (data from [16]) and 3.4 kbar (this work).

the resistance has dropped to about 3% R_{ns} from where it slowly converges to zero. This behavior might originate from inhomogenities within the sample. The sample imperfections can also make it more sensitive to the possible pressure inhomogenity.

During an initial test cooling sample #2 showed a rather clean behavior. The sample, however, was bicrystalline so we had to grind it. After the grinding the sample clearly showed signs of a chemical reaction with the brass ground plate. This might be the reason for the rather low quality of the sample estimated from the above mentioned measurements. Since the sample also showed unusual low critical fields we will exclude it for the rest of the discussion.

Fig. 5.20 shows the method used to determine critical field and temperature from the transition curves: The transition curve as well as the normal state resistance were fitted linearly at the inflection point. The point where the linear extrapolation of the normal state intersects with the fit to the transition, was taken as the upper critical field or the critical temperature, respectively. For the θ-dependence of critical field measurement also the point in the transition, where half of the normal state resistance is reached ("transition midpoint"), was examined.

However, for most transition curves the construction scheme changes the critical temperature/field dependence only by a constant offset, which is of no interest to us. Therefore mainly T_{cu} and B_{c2u} were used and therefore, if not explicitly mentioned otherwise the terms T_c and B_{c2} always refer to those values. According to Oh and Naughton [75] this determination anyway is the most correct for resistive measurements when compared to the critical fields obtained from magnetic torque measurements.

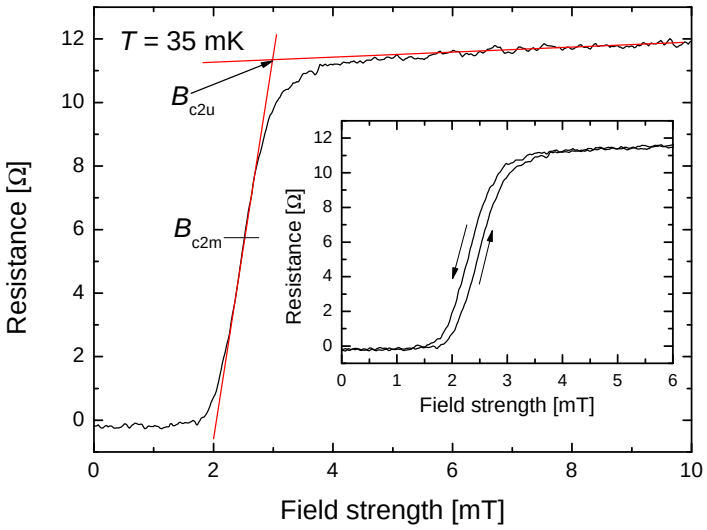

Figure 5.20: Possible constructions for the determination of the critical field (and critical temperature). The inset shows the hysteresis between up and down sweep.

Most measurements had hysteresis due to the time constant of the measurement, as shown in the inset of Fig. 5.20. For these cases the average value from both up and down sweeps was used.

In layered superconductors the magnetization curves for magnetic fields applied perpendicular to the layers often show a considerable reversible part near the upper critical field and the curves are smeared out due to fluctuations. Therefore the determination of the upper critical field is difficult and often results in the determination of the so called irreversibility field, a characteristic field considerably lower than H_{c2}, where the magnetization curves start to show hysteresis. The critical temperature of the superconductors under investigation in this work is very small ($T_c \sim 100$ mK). For that reason the influence of flux motion and fluctuations is strongly reduced and the critical fields determined by resistive measurements are the upper critical field or at least very near to H_{c2}.

5.3.2 Magnetic field perpendicular to the conducting layers

In order to determine the superconducting B-T phase diagram of α-(BEDT-TTF)$_2$ KHg(SCN)$_4$ for magnetic fields perpendicular to the layers, a series of field sweeps at different constant temperatures in the range from 23 mK up to 85 mK were done. As the perpendicular critical fields of α-(BEDT-TTF)$_2$KHg(SCN)$_4$ are very small, these sweeps were done in both the positive and negative field directions to make sure that the results are not falsified by any residual field.

In Fig. 5.21, which shows some of the curves taken in this experiment, we indeed observe a shift in the minima positions of about 0.08 mT to the negative side of the

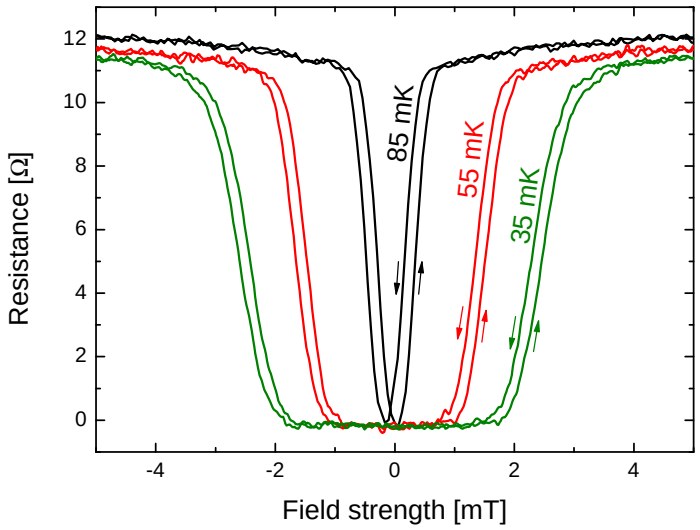

Figure 5.21: Transition curves at different temperatures for up and downsweeps (indicated the the arrows) in a magnetic field range between -5 and 5 mT.

field range. As this measurements were the first made after cooling down the magnet there should be no considerable remanent fields in the superconducting coil. The value of 0.08 mT is a factor of two stronger than the earth magnetic field and is probably due to magnetization of the steel reinforcement of the floor (induced by former high field measurements in the laboratory). This value could also be confirmed by measurements with a Hall sensor.

The B-T phase diagram can be seen in Fig. 5.22. The behavior is linear over the whole measured range, coresponding to a purely orbital pair breaking (as mentioned in section 2.2.1).

In Fig. 5.23 our data is compared to earlier measurements made by D. Andres et al. [7] and S. Jakob [16] at other pressures. As we can see, our pressure estimation of 3.4 kbar fits the scheme very well as our curve lies below the one obtained for 3.0 kbar and slightly above the 3.5 kbar curve.

From this phase diagram the Ginzburg-Landau coherence length parallel to the layers $\xi_{\parallel}(T)$ can be evaluated by extrapolating the data linearly to obtain $H_{c2,\perp}(T = 0) = 4.4$ mT. Using the Gl formula 2.6 we obtain

$$\xi_{\parallel,0} := \xi_{\parallel}(0) = \sqrt{\frac{\Phi_0}{2\pi B_{c2,\perp}(0)}} \approx 270\,\mathrm{nm}. \tag{5.7}$$

This value for $\xi_{\parallel,0}$ is a little higher than the value estimated by S. Jakob [16] for 2.8 kbar. That, however, could be expected as the critical temperature decreased and $\xi_0 \propto \frac{\hbar v_F}{k_b T_c}$.

This values now can be compared to the inplane mean free path, which can be estimated from the Fermi velocity and the scattering time of the sample. According to

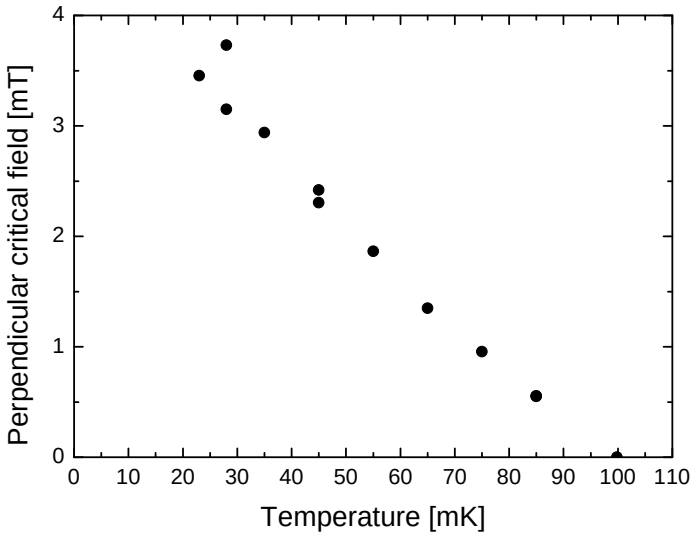

Figure 5.22: Phase diagram for a magnetic field perpendicular to the layers.

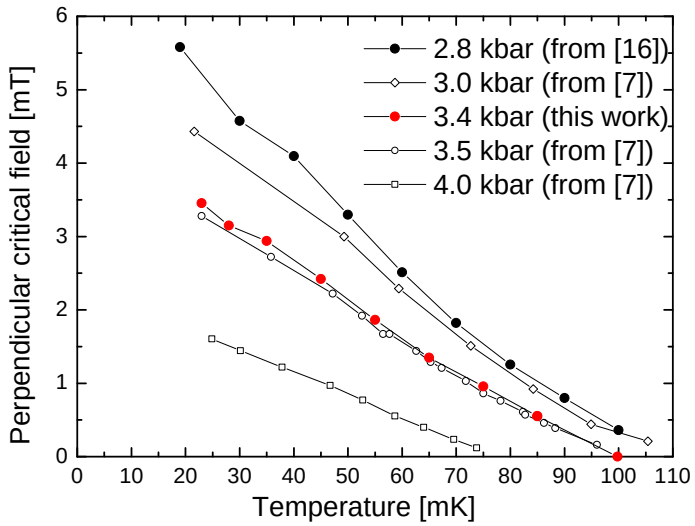

Figure 5.23: Phase diagram of α-(BEDT-TTF)$_2$KHg(SCN)$_4$ for different pressures comparing the recently acquired data with data collected by D. Andres et al. [7] and S. Jakob [16].

Wosnitza [52] the Fermi velocity can be calculated from the Fermi energy of α-(BEDT-TTF)$_2$KHg(SCN)$_4$ and the effective mass obtained by dHvA measurements, which has been done with this sample by Andres et al. [76]. Another possibility to estimate v_F are angle-dependent periodic orbit resonance measurements, which were performed by Kovalev et al. [77]. With both methods we obtain a value of

$$v_F \sim 10^5 \frac{\mathrm{m}}{\mathrm{s}}. \tag{5.8}$$

Furthermore, we need the scattering time τ, which we have estimated to 1.3 ps for both samples by determining the Dingle temperature from the high field SdH measurement mentioned in section 5.3.1. Now we can calculate the mean free path length

$$l_{\mathrm{mfp}} \approx \tau v_F = 110\,\mathrm{nm}, \tag{5.9}$$

which is less than one half of the coherence length, suggesting that we are rather in the dirty limit ($l_{mfp} < \xi_0$). However, the estimation of τ from the Dingle temperature gives only a lower limit [32]. In organic metals the transport τ can be almost an order of magnitude higher [78]. For sample #1 a much larger transport scattering time, $\tau = 15$ ps, has also been evaluated by Kartsovnik et al. using AMROs [55]. When calculating the mean free path with this value we get

$$l_{\mathrm{mfp}} \approx \tau v_F = 1250\,\mathrm{nm}, \tag{5.10}$$

which is more than four times as big as the coherence length of sample #1 meaning we are in the clean limit ($l_{mfp} \gg \xi_0$). This, however, is also a rough estimation. As the first estimation is a lower limit and the second a rough one we most probably have a mean free path somewhere in the intermediate regime between the clean and dirty limits.

5.3.3 Magnetic field parallel to the conducting layers

While for perpendicular magnetic fields the behavior of α-(BEDT-TTF)$_2$KHg(SCN)$_4$ is very similar to bulk superconductors it changes dramatically when magnetic field is applied parallel to the conducting layers.

In order to obtain the B-T phase diagram for the parallel field orientation, measurements were performed at azimuthal angles $\varphi = 38°$, where the highest critical fields are observed, and $\varphi = 118°$, near the minimum for critical fields in parallel direction. (A more detailed investigation on the azimuthal anisotropy of our compound will be presented in section 5.3.4.) The data was obtained from both field sweeps at constant temperature and temperature sweeps at constant field. As will be shown below (section 5.3.5), the present layered superconductor is extremely sensitive to the exact alignment of the field for field orientations nearly parallel to the layers. Therefore, it was necessary to determine the exact parallel direction and adjust the field direction accordingly before doing the measurements. For this purpose, sweeps of the θ-angle were done at a constant temperature and field fixed somewhere in the middle of the superconducting transition of the sample. An example of such θ-sweeps is shown in Fig. 5.24. We see

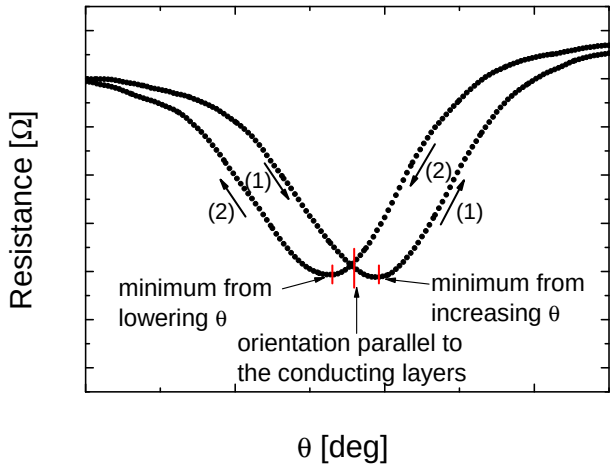

Figure 5.24: Determination of the parallel orientation: the minima of the sweeps in positive (1) and negative (2) angular direction were averaged to obtain the exact parallel field orientation (taken from [16]).

a dip in the resistance with the center being the θ-angle, where the field is oriented parallel to the layers. As presented in Fig. 5.24, there is a weak hysteresis between up and down sweeps. Therefore, the parallel position was determined by taking the average of the two minima.

Some examples for field sweeps at different temperatures and temperature sweeps at different fields are given in Fig. 5.25 (a) and (b), respectively. In Fig. 5.26 the phase diagram for both azimuthal angles, $\varphi = 38°$ and $\varphi = 118°$ is shown. Both curves are linear near T_c and start bending at about 90 mK. Also both curves tend to saturation

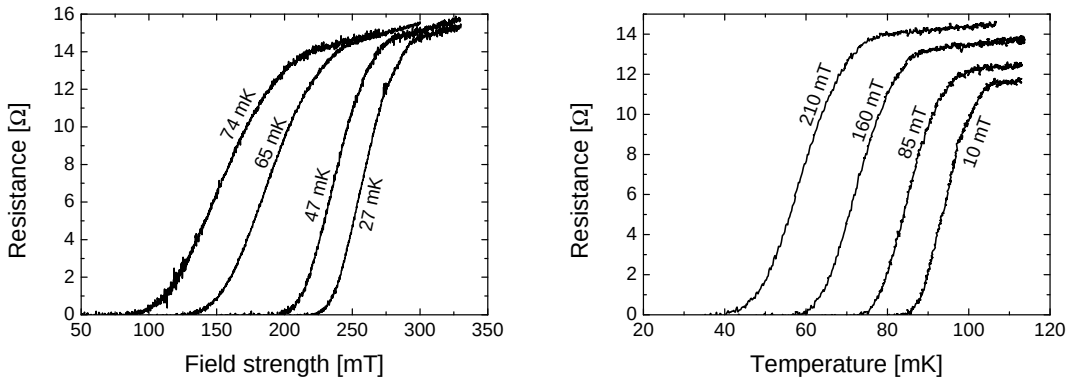

Figure 5.25: (a) Field sweeps with magnetic field parallel to the layers at different temperatures. (b) Temperature sweeps at different magnetic fields aligned parallel to the layers.

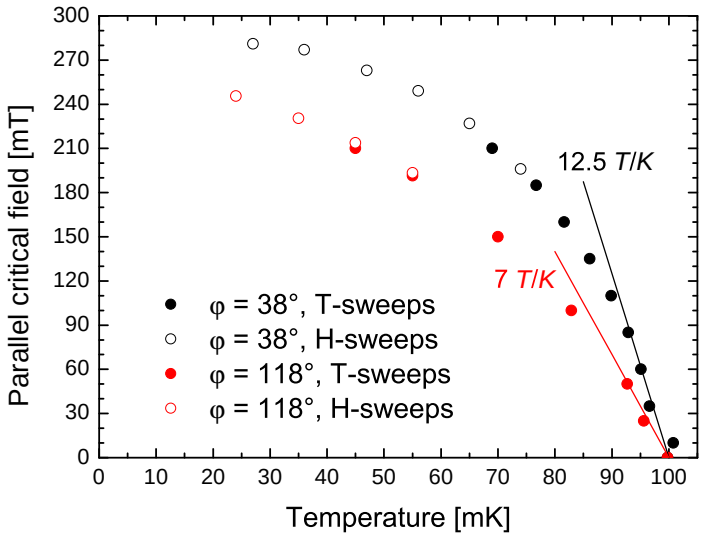

Figure 5.26: B-T phase diagram for fields parallel to the layers at different azimuthal angles.

at a field of slightly less than 290 mT. Whereas the curve for $\varphi = 38°$ almost reaches the saturation value at $T = 27$ mK, the curve for $\varphi = 118°$ is still growing down to that temperature.

From the slope of the linear part of the $B_{c2}(T)$-dependence the Ginzburg-Landau coherence length in perpendicular direction $\xi_{\perp,0}$ can be calculated for both azimuthal angles by using the value of $\xi_{\parallel,0}$ evaluated in section 5.3.2 using equation 2.8.

For $\varphi = 38°$ the slope of the linear part is $dB_{c2,\parallel}/dT = 12.5\,\mathrm{K/T}$. Therefore, the coherence length is

$$\xi_{\perp,0} = \frac{\Phi_0}{2\pi\xi_{\parallel,0}(dB_{c2,\parallel}/dT)T_c(0)} \approx 1.0\,\mathrm{nm}. \tag{5.11}$$

For $\varphi = 118°$ we have a slope of $7.0\,\mathrm{K/T}$ in the linear part resulting in a coherence length of

$$\xi_{\perp,0} \approx 1.8\,\mathrm{nm}, \tag{5.12}$$

Of course, $\xi_{\perp,0}$ cannot have two different values at the same time. The mismatch between the two values most likely originates from an anisotropy of $\xi_{\parallel,0}$ in φ. The value for $\xi_{\parallel,0}$ we obtained in section 5.3.2 is an average over all φ-directions. Thus, the true value for the the perpendicular coherence length most likely is an average of the two values estimated above:

$$\xi_{\perp,0} \approx 1.4\,\mathrm{nm} \tag{5.13}$$

This value is equal to $\frac{d}{\sqrt{2}} \approx 1.4\,\mathrm{nm}$ and, therefore, our system can be considered to be on the border to the q2D regime at $T = 0$. However, as the coherence length grows with

increasing temperature, diverging at T_c according to Eq. (2.2)), the sample definitely is in a 3D state during the linear part and the pair breaking is due to orbital effect.

With the slope near T_c we can estimate the Maki parameter, which gives a measure for the influence of the Pauli paramagnetic effect. In our case we get $\alpha \approx B_{c2}^{orb}(0)/B_{\mathrm{CC-limit}} = 6.7$ for $\varphi = 38°$ and $\alpha = 3.8$ for $\varphi = 118°$. That means for both directions we expect a strong influence of the paramagnetic effect. This is directly seen by the strong bending of the initial slope coming almost to saturation at low temperature.

A strong argument in favor of a Pauli-paramagnetic pair breaking mechanism is given by the temperature dependence of the azimuthal anisotropy. Near T_c it is given by the different slopes in Fig. 5.26 and amounts to a factor of almost 2. As mentioned above the corresponding φ-angles correspond to maximal and minimal values of the inplane critical fields. When we now look at the temperature dependence, we see that it decreases with decreasing temperature. A rough extrapolation to $T = 0$ yields almost the same value for both inplane directions. This is what we would expect as the Pauli-mechanism is angle-independent.

Another noteworthy result of our measurements is that the Chandrasekhar-Clogston paramagnetic limit (Eq. (2.16)) is exceeded by a factor of ~ 1.5. Fig. 5.27 shows both curves, where T is normalised to T_c and the critical field to the value of the CC-limit (filled circles). The plot also shows the normalised data obtained by S. Jakob at 2.8 kbar (empty circles), which exceeds the CC-limit by about the same value. This large discrepancy between the theoretically estimated CC-limit and the measured value

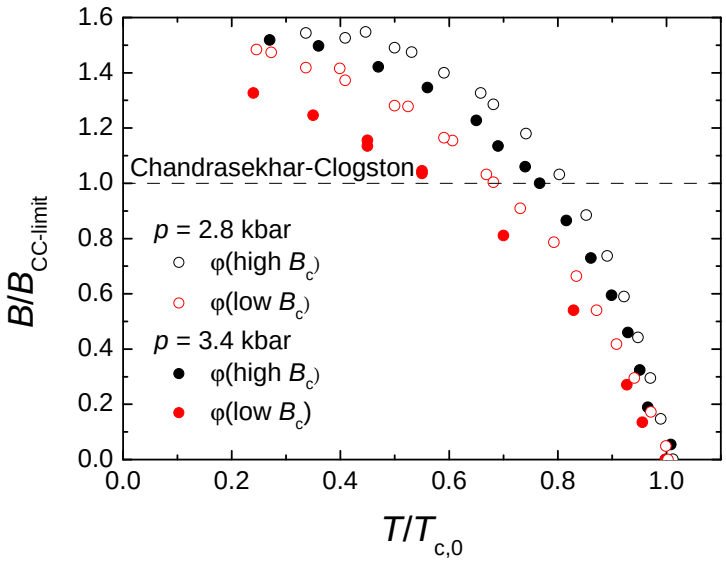

Figure 5.27: Comparison of the presently obtained data at 3.4 kbar with the former data at 2.8 kbar (from [16]). All curves have been normalised, the temperature to T_c and the critical field to the Chandrasekhar-Clogston limit.

of the paramagnetic limit most probably originates from an enhanced energy gap Δ. The calculations by Chandrasekhar and Clogston assume the BCS value for Δ. In organic superconductors the energy gap is strongly enhanced by strong electron-phonon and electron-electron coupling compared to the BCS value. There even are organic superconductors exceeding the CC-limit by up to a factor of 2 [79].

Because of its very high anisotropy and the fact that we are able to reach the paramagnetic limit α-(BEDT-TTF)$_2$KHg(SCN)$_4$ is also seen as a candidate for showing a FFLO superconducting state (see section 2.2.3). But no clear sign for a FFLO state could be discovered in our data. This, however, is not surprising as it is very hard to trace a transition into a FFLO state from resistive measurements. Furthermore, the lowest temperature used in this experiment probably still is too high for the appearance of a FFLO state.

Comparing the above estimations for the parallel field with those from the perpendicular field, we can say that even though α-(BEDT-TTF)$_2$KHg(SCN)$_4$ can be considered to be a 3D superconductor over the whole T range at this pressure, it has a very high anisotropy parameter (equation 2.9)

$$\gamma = \frac{\xi_{\parallel,0}}{\xi_{\perp,0}} = 193. \tag{5.14}$$

This value is a little lower than the one evaluated at 2.8 kbar but still very high compared to values obtained for other organic superconductors from critical field experiments.

We can also estimate the anisotropy parameter from the transfer integrals $t_\perp$ and $t_\parallel$,

$$\gamma = \left(\frac{m_\perp}{m_\parallel}\right)^{\frac{1}{2}} = \frac{t_\parallel a}{t_\perp d}, \tag{5.15}$$

with the crystal lattice periods within and across the layers $a \approx 10$Å and $d \approx 20$Å [50], respectively. With this relation and values of the transfer integrals taken from [55] we can now evaluate the anisotropy parameter as

$$\gamma = \frac{t_\parallel a}{t_\perp d} \approx 200, \tag{5.16}$$

which is in excellent agreement with the measured values.

5.3.4 φ-dependence of critical field parallel to the layers

As we have seen in the last section α-(BEDT-TTF)$_2$KHg(SCN)$_4$ not only shows anisotropic behavior for magnetic fields applied perpendicular or parallel to the layers, but also when applying parallel field in different azimuthal angles φ. This azimuthal anisotropy will now be more closely investigated. For that purpose a first rough estimation was done in the same way as during the ambient pressure measurements (section 5.2.3). Therefore, temperature and field were chosen so that the sample resistance was approximately half the normal state resistance in exact parallel field direction for the starting φ and then angular sweeps of the θ angles were done in the window of $\pm 5^\circ$

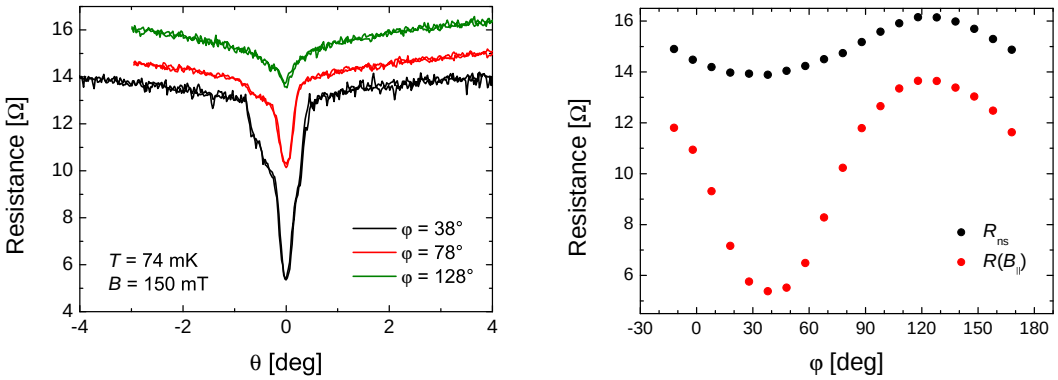

Figure 5.28: (a) Examples of θ-sweeps at different φ. (b) Normal state magnetoresistance R_{ns} and resistance in the parallel direction $R(B_{\parallel})$ (the dips of the θ sweeps) as a function of φ. $T = 74$ mK and $B = 150$ mT for all sweeps.

around the parallel orientation in steps of $\Delta\varphi = 10°$. The temperature was chosen to $T = 74$ mK and the magnetic field was set to $B = 150$ mT.

In Fig. 5.28 (a) we can see some examples of θ-sweeps at different φ angles, which show rather different behavior. The φ-dependence of the normal state resistance and the resistance at the field orientation exactly in the dip are shown in Fig. 5.28 (b). However, only a qualitative view of the critical field can be obtained this way.

To get a better idea of the azimuthal anisotropy of the critical field, field sweeps at different φ-angles with a step size of 10° were done at $T = 35$ mK. For each φ the parallel field direction first had to be determined the same way as in section 5.3.3. Some examples of the field strength sweeps can be seen in Fig. 5.29.

The resulting critical field behavior is shown in Fig. 5.30. Like in section 5.2.3, the hollow circles are from the same data as the filled ones but have been shifted by 180° to get a clearer idea of the behavior over the whole angular range, as the points were only measured in an interval of 190°.

We can see that our data shows some scattering, especially in the region of the extrema. A reason for this could be the difficulty in determining the exact parallel orientation, because some θ-sweeps showed rather broad dips with some additional features. And, as we will discuss in section 5.3.5, for parallel orientation of the field even very small changes in the angle have a huge effect on the critical field.

The sample shows an increase of the critical field of $\approx 20\%$ from the angle with lowest value to the one with the highest value and a periocidity of 180°. Therefore we do not have a hint for a d-wave pairing in α-(BEDT-TTF)$_2$KHg(SCN)$_4$, because a d-wave, which was proposed for organic superconductors in a vicinity of a density wave instability, is expected to show itself in a four-fold symmetrie [80–82].

These results are in good agreement with the measurements of the parallel critical field at $\varphi = 38°$ and $\varphi = 118°$ in section 5.3.3. As we can see in the B-T phase diagram Fig. 5.26, the critical field for the two inplane directions differ by about 20%. At this

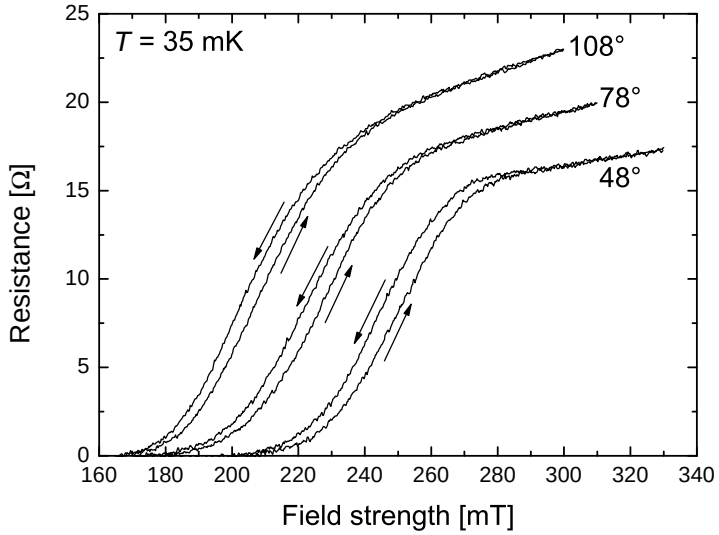

Figure 5.29: Three transition curves recorded at different values of φ showing both up and down sweeps as indicated by the arrows. The magnetic field is applied exactly parallel to the layers and $T = 35$ mK.

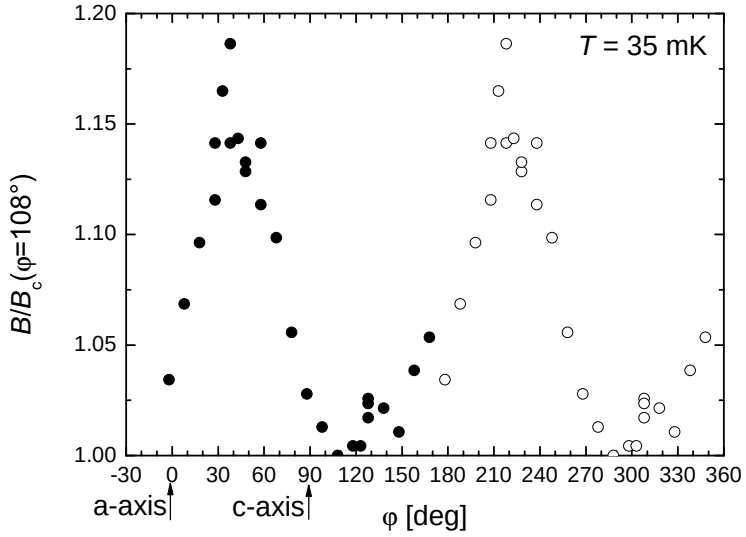

Figure 5.30: φ-dependence of the inplane critical field, with $\varphi = 0°$ corresponding to field aligned parallel to the a-axis at $T = 35$ mK.

low temperature of 35 mK we already have a contribution from the Pauli-paramagnetic pair breaking effect, whereas the anisotropy derived from the slope near T_c was much higher as discussed above.

We can compare this behavior to the one obtained at ambient pressure (Fig. 5.13. There we can see that the φ with the highest critical field, is shifted by $\approx 15°$ between $p = 0$ kbar and 3.4 kbar. As the measurement at 0 kbar yields only very rough results the existence of the shift is questionable. This suggests that the same electrons systems are responsible for superconductivity at both pressure values. This is remarkable, considering that the high pressure state of α-(BEDT-TTF)$_2$KHg(SCN)$_4$ has a completely changed electron system compared to ambient pressure, as is indicated by the shifted behavior of the normal state magnetoresistance (compare Fig. 5.13 (a) to Fig. 5.28 (b)).

When comparing our results with the data at $p = 2.8$ kbar [16] we can see that the shift in position of the peaks and dips is within the error bar of the angle determination. But as the older measurements were performed using temperature sweeps at constant field the two data sets are not really comparable and, therefore, no more information can be obtained this way.

5.3.5 θ-dependence of the critical field

Further, a more detailed investigation of the anisotropic behavior of the critical field depending on the polar angle θ was performed. The whole series of measurements was done at $\varphi = 38°$, where we had estimated the highest critical field in parallel direction. Field sweeps at different θ-angles were done in a range of $-90° \leq \theta \leq +90°$, with $\theta = 0°$ being the direction where the magnetic field is parallel to the layers, at temperatures of 35 mK, 65 mK and 90 mK.

Some examples of transition curves at 35 mK and 90 mK are given in Fig. 5.31. For $T = 35$ mK the curves show a sharp transition for all θ values. The curves obtained from $T = 65$ mK (not shown) look rather similar to those at 35 mK with the transitions

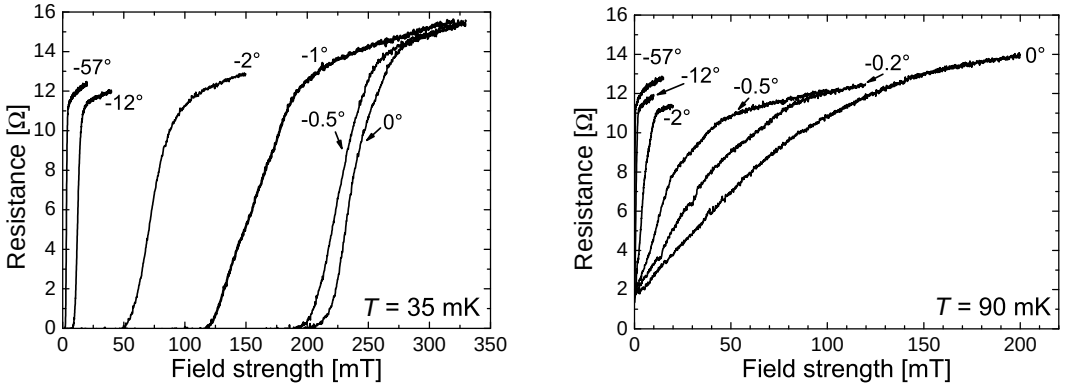

(a) (b)

Figure 5.31: Examples of field-sweeps at different θ, (a) $T = 35$ mK (b) $T = 90$ mK.

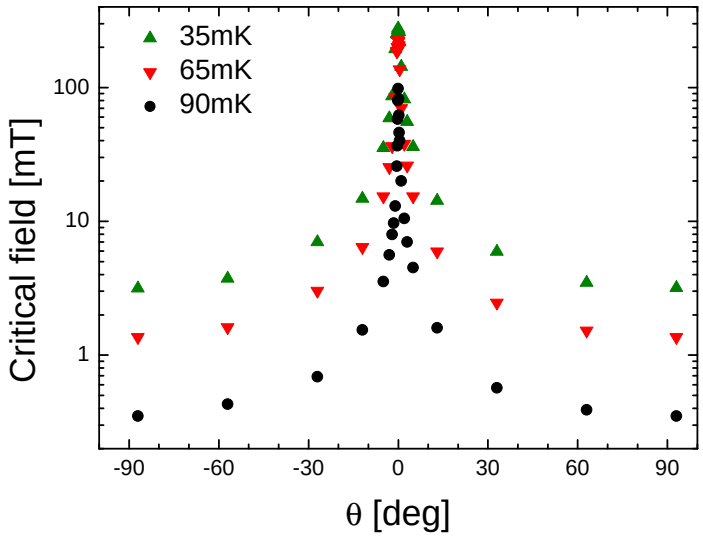

Figure 5.32: θ-dependence of the critical field at $T = 35$ mK, 65 mK and 90 mK.

shifted to somewhat lower temperatures. At $T = 90$ mK the sample is not completely superconducting even at $B = 0$, therefore the transition always starts at a finite resistance value, but the slope changes with θ. For $\theta \to 0°$ the transitions become very broad and the error bar for the obtained B_{c2} value is rather large. But even qualitatively one sees from Fig. 5.31 (b) that B_{c2} is extremely sensitive to θ in this region: A strong angular dependence appears in the curves for $\theta = 0.5°$, $0.2°$ and $0°$. Because our standard construction for B_{c2} (presented at the end of section 5.3.1) was difficult to apply, the dependence was also determined with the "transition midpoint" criterion. For both criteria we obtained the same relative dependence. Therefore we show the data with the standard construction in the graphs.

The θ-dependence of the critical field can be seen in Fig. 5.32. Note that the plots are in logarithmic scale, otherwise the behavior for high absolute values of θ could not be resolved. The huge anisotropy over the θ-range can be clearly seen.

In Fig. 5.33 the curves for all temperatures are normalised to their respective perpendicular critical field value. Here we can see that for $|\theta| \gtrsim 1°$ all curves behave the same and over most of the angular range coincide well with fits by the LD-model for highly anisotropic 3D superconductors (Eq. (2.10)) and the equation for q2D superconductors from Tinkham (Eq. (2.12)). The fit of the Tinkham formula, however, is not shown in Fig. 5.33 as it would be indistinguishable from the fit of the LD-model. This is a sign that in this θ-range the orbital effect is dominant for all temperatures.

Therefore we take a closer look to the range of $|\theta| \leq \pm 5°$, shown in Fig. 5.34. The $T = 90$ mK curve shows a very sharp peak at $\theta = 0°$ and we have the highest anisotropy. From this we can draw the conclusion that we are in a temperature regime, where the orbital effect is the dominant pair breaking mechanism for all θ-angles.

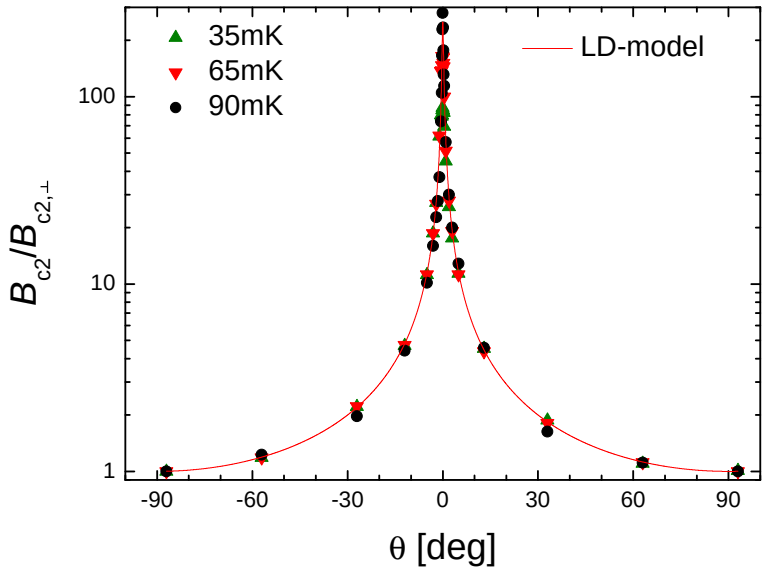

Figure 5.33: θ-dependence of critical field normalised to the perpendicular critical field at 35 mK, 65 mK and 90 mK. The red line is a fit to the $T = 90$ mK data with the LD-model 2.10.

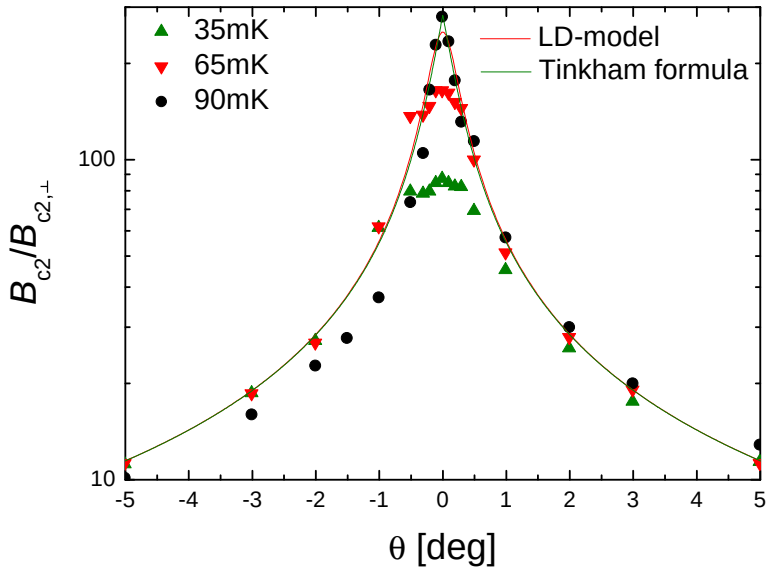

Figure 5.34: Data from Fig. 5.33 in the range of $-5° < \theta < +5°$. The $T = 90$ mK curve has been fitted with the LD-model 2.10 (red line) and the Tinkham formula 2.12 (green line)

At this temperature we obtain an anisotropy of

$$\frac{B_{c2,\parallel}}{B_{c2,\perp}} = 280 \quad \text{for} \quad T = 90\,\text{mK}.$$

As we have only little contributions due to the Pauli-effect the above calculated value is a good estimation for the anisotropy parameter $\gamma = 280$. This value is the highest anisotropy of B_{c2} ever obtained in organic superconductors. It is also much higher than the value of $\gamma = 193 \ll 280$ (Eq. 5.14), obtained from the comparison of the slopes of $B_{c2}(T)$ near T_c. However, there we have calculated an average value of γ for both measured φ-directions. When we only use the slope of the phase diagram for $\varphi = 38°$, which was the angle with the highest $B_{c2,\parallel}$ and also the angle, where the whole θ-dependence experiment was done, we obtain a value of $\gamma = 284$ from the slopes. So the two sets of measurements are in excellent agreement with each other.

In this field range also the fits from both the LD-model and the Tinkham formula for $T = 90$ mK are shown (Fig. 5.34). We can see that at such huge anisotropies the theoretical curves only differ for $|\theta| \leq 0.2°$.

The LD-fit provides a value for the anisotropy of 251, which is rather an underestimation. The anisotropy value provided by the Tinkham-fit is 284, which is in excellent agreement with the measured value. This is very reasonable as it fits the complete θ-range very well including the point at $\theta = 0°$. Therefore, the Tinkham-fit looks a bit more reliable. The deviation from the data, which both fits show in the range of $-5° < \theta < -1°$ cannot be explained.

For the lower temperatures the anisotropy decreases as we can see in the ratio of the parallel and perpendicular critical field:

$$\frac{B_{c2,\parallel}}{B_{c2,\perp}} = 165 \quad \text{for} \quad T = 65\,\text{mK}$$

$$\frac{B_{c2,\parallel}}{B_{c2,\perp}} = 87 \quad \text{for} \quad T = 35\,\text{mK}$$

In addition the peaks are flattened and we almost have a plateau around $\theta = 0°$. This could be expected in the case of a reduction of the critical field by the Pauli paramagnetism: The paramagnetic limit is angle-independent, so for all θ-angles, where the Pauli-effect is the main pair breaking mechanism, B_{c2} is more or less θ-independent. Another possible explanation for such a plateau might be a redirection of the magnetic flux lines through flux vortices, which cross the superconductor in a direction exactly parallel to the layers. In that case a jump of the critical field value at the edges of the plateau would be expected. However, such a jump is not visible in our data. This leaves the Pauli paramagnetic effect as the only possible explanation for the behavior of $B_{c2}(\theta)$. This is yet the most prominent evidence of the paramagnetic pair breaking effect ever obtained.

6 Summary

The subject of this diploma thesis was the study of normal state and superconducting properties at the border between a charge-density wave (CDW) and superconducting states in the organic metal α-(BEDT-TTF)$_2$KHg(SCN)$_4$. In this compound at very low temperature, a pressure of about $p_c \approx 2.5$ kbar leads a to a transition from the CDW to the superconducting ground state.

We investigated the pressure dependence of the effective cyclotron mass in α-(BEDT-TTF)$_2$KHg(SCN)$_4$, using Shubnikov-de Haas oscillations between $p = 0$ and 8 kbar. A maximum of $m_c(p) = 1.76\, m_e$ was found at $p \approx 5$ kbar. This pressure value deviates from the critical pressure of the transition between CDW and normal metallic state, $p_c \approx 2.5$ kbar, observed at $B = 0$. As the data was taken at $B > 11$ T, the field-induced CDW (FICDW) state at $p > 2.5$ kbar should be taken into consideration. The enhancement of m_c around $p \approx 5$ kbar suggests that this pressure value is the critical pressure for the FICDW state in this field range.

For the investigation of the superconducting state only very small fields are necessary and the FICDW state should play no role. Former experiments at $p = 2.8$ kbar have shown a very anisotropic behavior of the critical field depending on the field direction. An estimation of the pressure dependence should be accomplished by a similar study further away from the critical pressure. For the present study $p = 3.4$ kbar was chosen.

The zero-field critical temperature was determined to $T_c = 100$ mK. For fields perpendicular to the conducting layers a B-T phase diagram was obtained, which clearly shows the behavior expected for an orbital pair breaking effect. The in-plane coherence length was estimated to $\xi_{\parallel,0} \approx 270$ nm.

The B-T phase diagram obtained for fields in the direction parallel to the layers shows a very steep slope near T_c with up to 12.5 T/K, which suggests Pauli-paramagnetism as dominant pair breaking effect for temperatures below 70 mK. The Chandrasekhar-Clogston paramagnetic limit is exceeded by a factor of 1.5. We can, therefore, suggest that the superconducting energy gap in our compound is enhanced by strong electron-phonon and electron-electron coupling as compared to the BCS value. The coherence length perpendicular to the layers was estimated to $\xi_{\perp,0} \approx 1.4$ nm. Therefore, we have an anisotropy parameter of $\gamma = \xi_{\parallel,0}/\xi_{\perp,0} \approx 200$. This is by far the largest value for γ so far measured from critical field experiments in any known layered superconductor.

The dependence of the critical field on the polar angle θ was examined at different temperatures. At temperatures near T_c the critical field is dominated by the orbital effect even for fields parallel to the layers. The critical field shows a very sharp peak for this field direction. An anisotropy of the critical field between parallel and perpendicular orientations of 280 was obtained. For lower temperatures we receive a plateau in the θ dependence of the critical field for a θ range of $\sim \pm 0.5^\circ$ around the parallel ori-

entation. The temperature dependence of this behavior provides a prominent evidence for a paramagnetic pair breaking.

We have also investigated the dependence of the inplane critical field of α-(BEDT-TTF)$_2$ KHg(SCN)$_4$ on the azimuthal orientation φ. It also shows a considerable anisotropy being the highest near T_c, where we observe almost a factor of 2 difference between the minimal and the maximal slopes dH_{c2}/dT near T_c.

In comparison to the earlier experiments at 2.8 kbar, the anisotropy of superconductivity has decreased. This could be expected, since our compound like many organic compounds shows enhanced interlayer transport under hydrostatic pressure resulting in a more 3D behavior. Corncerning the parallel critical fields we found that the slope near T_c is considerably reduced by increasing the pressure, but the low temperature value did not change in coordinates normalised to the critical field. The general behavior of the azimuthal anisotropy obtained in our work is found to be in good agreement with the experiment at $p = 2.8$ kbar.

Because of the appearance of the paramagnetic effect, α-(BEDT-TTF)$_2$KHg(SCN)$_4$ is also seen as a candidate for showing a FFLO superconducting state. However, no hints for it have been found yet. Further measurements under even lower temperatures and with other methods would be required to clarify this issue.

Bibliography

[1] J. G. Bednorz & K. A. Müller. Possible high-T_c superconductivity in the Ba-La-Cu-O system. *Zeitschrift für Physik B Condensed Matter* **64**, 189–193 (1986). URL http://dx.doi.org/10.1007/BF01303701. 10.1007/BF01303701.

[2] Proceedings of the 22nd International Symposium on Superconductivity. *Physica C: Superconductivity* **470** (20), (2010).

[3] S. Anders, M. Blamire, F.-I. Buchholz, D.-G. Crété, R. Cristiano, P. Febvre, L. Fritzsch, A. Herr, E. Il'ichev, J. Kohlmann, J. Kunert, H.-G. Meyer, J. Niemeyer, T. Ortlepp, H. Rogalla, T. Schurig, M. Siegel, R. Stolz, E. Tarte, H. ter Brake, H. Toepfer, J.-C. Villegier, A. Zagoskin & A. Zorin. European roadmap on superconductive electronics - status and perspectives. *Physica C: Superconductivity* **470**, 2079 – 2126 (2010). URL http://www.sciencedirect.com/science/article/pii/S0921453410005332.

[4] The 23rd International Symposium on Superconductivit. *Physica C: Superconductivity* **471** (21-22), (2011).

[5] J. Schmalian. Unkonventionell und komplex. *Physik Journal* **10**, 37–43 (2011). URL http://www.pro-physik.de/details/physikjournalArticle/1097815/Unkonventionell_und_komplex.html.

[6] H. Taniguchi, M. Miyashita, K. Uchiyama, K. Satoh, N. Môri, H. Okamoto, K. Miyagawa, K. Kanoda, M. Hedo & Y. Uwatoko. Superconductivity at 14.2 K in Layered Organics under Extreme Pressure. *Journal of the Physical Society of Japan* **72**, 468–471 (2003). URL http://jpsj.ipap.jp/link?JPSJ/72/468/.

[7] D. Andres, M. V. Kartsovnik, W. Biberacher, K. Neumaier, E. Schuberth & H. Müller. Superconductivity in the charge-density-wave state of the organic metal α-(BEDT-TTF)$_2$MHg(SCN)$_4$. *Phys. Rev. B* **72**, 174513 (2005). URL http://link.aps.org/doi/10.1103/PhysRevB.72.174513.

[8] P. Christ, W. Biberacher, M. Kartsovnik, E. Steep, E. Balthes, H. Weiss & H. Müller. Magnetic field-temperature phase diagram of the organic conductor α-(BEDT-TTF)$_2$KHg(SCN)$_4$. *JETP Lett.* **71**, 303 (2000).

[9] N. Biskup, J. Perenboom, J. Brooks & J. Qualls. Argument for charge density wave sub-phases in the ground state of α-(BEDT-TTF)$_2$KHg(SCN)$_4$. *Solid State Communications* **107**, 503 – 507 (1998). URL http://www.sciencedirect.com/science/article/pii/S003810989800252X.

[10] N. Harrison, L. Balicas, J. S. Brooks & M. Tokumoto. Critical state in a low-dimensional metal induced by strong magnetic fields. *Phys. Rev. B* **62**, 14212–14223 (2000). URL http://link.aps.org/doi/10.1103/PhysRevB.62.14212.

[11] M. V. Kartsovnik, D. Andres & W. Biberacher. Hierarchy of the density-wave states and superconductivity in the organic conductor α-(BEDT-TTF)$_2$KHg(SCN)$_4$. *Comptes Rendus Chimie* **10**, 6 – 14 (2007). URL http://www.sciencedirect.com/science/article/pii/S1631074806001500.

[12] M. Kartsovnik, D. Andres, W. Biberacher, P. Christ, E. Steep, E. Balthes, H. Weiss, H. Müller & N. Kushch. B-T-p phase diagram of α-(BEDT-TTF)$_2$KHg(SCN)$_4$. *Synthetic Metals* **120**, 687 – 690 (2001). URL http://www.sciencedirect.com/science/article/pii/S0379677900011188. Proceedings of the International Conference on the Science and Technology of Synthetic Metals.

[13] D. Andres, M. V. Kartsovnik, W. Biberacher, H. Weiss, E. Balthes, H. Müller & N. Kushch. Orbital effect of a magnetic field on the low-temperature state in the organic metal $\alpha - (\mathrm{BEDT-TTF})_2\mathrm{KHg(SCN)}_4$. *Phys. Rev. B* **64**, 161104 (2001). URL http://link.aps.org/doi/10.1103/PhysRevB.64.161104.

[14] D. Andres, M.V. Kartsovnik, W. Biberacher, K. Neumaier & H. Müller. Direct evidence for superconductivity in the organic charge density wave compound α-(BEDT-TTF)$_2$KHg(SCN)$_4$ under hydrostatic pressure. *J. Phys. IV France* **12**, 87–88 (2002). URL http://dx.doi.org/10.1051/jp4:20020364.

[15] D. Andres. *Effects of High Magnetic Fields and Hydrostatic Pressure on the Low-Temperature Density-Wave State of the Organic Metal* $\alpha - (BEDT-TTF)_2KHg(SCN)_4$. Ph.D. thesis, Technische Universität München (2004).

[16] S. Jakob. *Magnetic field effects in the layered organic superconductor* $\alpha-(BEDT-TTF)_2KHg(SCN)_4$. Diplomarbeit, Technische Universität München (2007).

[17] M. Tinkham. *Introduction to Superconductivity* (Dover Puplications, Inc., (1996)), 2nd edn.

[18] V. V. Schmidt, P. Müller & A. V. Ustinov. *The Physics of Superconductors* (Springer-Verlag, (Berlin Heidelberg, 1997)).

[19] R. Gross & A. Marx, *Festkörperphysik Vorlesungsskript*. chap. 13 Supraleitung (2010). URL http://www.wmi.badw.de/teaching/Lecturenotes/FKP/FKP_Kapitel13.pdfl.

[20] E. Helfand & N. R. Werthamer. Temperature and Purity Dependence of the Superconducting Critical Field, H_{c2}. II. *Phys. Rev.* **147**, 288–294 (1966). URL http://link.aps.org/doi/10.1103/PhysRev.147.288.

[21] W. E. Lawrence & S. Doniach. Theory of layer structure superconductors. In *Proceedings of the 12th International Conference of Low-Temperature Physics* 361–362 (Kyoto, 1970).

[22] R. A. Klemm, A. Luther & M. R. Beasley. Theory of the upper critical field in layered superconductors. *Phys. Rev. B* **12**, 877–891 (1975). URL `http://link.aps.org/doi/10.1103/PhysRevB.12.877`.

[23] L. N. Bulaevskiĭ. Magnetic properties of layered superconductors with weak interaction between layers. *Sov. Phys.-JETP* **37**, 1133–1136 (1973).

[24] L. N. Bulaevskiĭ. Inhomogeneous state and the anisotropy of the upper critical field in layered superconductors with josephson layer interaction. *Sov. Phys.-JETP* **38**, 634–639 (1974).

[25] S. T. Ruggiero, T. W. Barbee & M. R. Beasley. Superconductivity in Quasi-Two-Dimensional Layered Composites. *Phys. Rev. Lett.* **45**, 1299–1302 (1980). URL `http://link.aps.org/doi/10.1103/PhysRevLett.45.1299`.

[26] B. S. Chandrasekhar. A note on the maximum critical field of high-filed superconductors. *Appl. Phys. Lett.* **1**, 7–8 (1962). URL `http://dx.doi.org/10.1063/1.1777362`.

[27] A. M. Clogston. Upper Limit for the Critical Field in Hard Superconductors. *Phys. Rev. Lett.* **9**, 266–267 (1962). URL `http://link.aps.org/doi/10.1103/PhysRevLett.9.266`.

[28] P. Fulde & R. A. Ferrell. Superconductivity in a Strong Spin-Exchange Field. *Phys. Rev.* **135**, A550–A563 (1964). URL `http://link.aps.org/doi/10.1103/PhysRev.135.A550`.

[29] A. Larkin & Y. Ovchinnikov. Inhomogenous state of superconductors. *Sov. Phys.-JETP* **20**, 762 (1965).

[30] K. Maki & T. Tsuneto. Pauli Paramagnetism and Superconducting State. *Progress of Theoretical Physics* **31**, 945–956 (1964). URL `http://ptp.ipap.jp/link?PTP/31/945/`.

[31] B. Bergk, A. Demuer, I. Sheikin, Y. Wang, J. Wosnitza, Y. Nakazawa & R. Lortz. Magnetic torque evidence for the Fulde-Ferrell-Larkin-Ovchinnikov state in the layered organic superconductor $\kappa - (\mathrm{BEDT-TTF})_2\mathrm{Cu(NCS)}_2$. *Phys. Rev. B* **83**, 064506 (2011). URL `http://link.aps.org/doi/10.1103/PhysRevB.83.064506`.

[32] D. Shoenberg. *Magnetic oscillations in metals* (Cambridge University Press, 1984).

[33] M. V. Kartsovnik. High Magnetic Fields: A Tool for Studying Electronic Properties of Layered Organic Metals. *Chem. Rev.* **104**, 5737–5782 (2004). URL `http://pubs.acs.org/doi/pdf/10.1021/cr0306891`.

[34] M. V. Kartsovnik, *The Physics of Organic Superconductors and Conductors*. A. G. Lebed (ed.), chap. 8, Layered Organic Conductors in Strong Magnetic Fields, 185–246 (Springer Verlag, 2008), 2nd edn.

[35] L. D. Landau. Diamagnetismus der Metalle. *Z. Phys.* **64**, 629–637 (1930).

[36] L. Onsager. Interpretation of the de Haas-van Alphen effect. *Phil. Mag.* **43**, 1006–1008 (1952).

[37] W. J. de Haas & P. M. van Alphen. *Proc. Netherlands Roy. Acad. Sci.* **33**, 1106 (1930).

[38] L. W. Shubnikov & W. J. de Haas. *Proc. Netherlands Roy. Acad. Sci.* **33**, 130 and 163 (1930).

[39] I. M. Lifshitz & A. M. Kosevich. *Sov. Phys.-JETP* **2**, 636 (1956).

[40] A. B. Pippard. *The Dynamics of Conduction Electrons* (Gordon and Breach, New York, 1965).

[41] A. B. Pippard. *Magnetoresistance in Metals* (Cambridge University Press, Cambridge, 1989).

[42] R. B. Dingle. Some Magnetic Properties of Metals. II. The Influence of Collisions on the Magnetic Behaviour of Large Systems. *Proc. Roy. Soc.* **211**, 517–525 (1952).

[43] D. Shoenberg. Magnetization of a two-dimensional electron gas. *Journal of Low Temperature Physics* **56**, 417–440 (1984). URL `http://dx.doi.org/10.1007/BF00681804`. 10.1007/BF00681804.

[44] A. G. Lebed. Anisotropy of an instability for a spin density wave induced by a magnetic field in a q1d conductor. *Sov. Phys.-JETP* **43**, 174–177 (1986).

[45] T. Osada, S. Kagoshima & N. Miura. Resonance effect in magnetotransport anisotropy of quasi-one-dimensional conductors. *Phys. Rev. B* **46**, 1812–1815 (1992). URL `http://link.aps.org/doi/10.1103/PhysRevB.46.1812`.

[46] M. V. Kartsovnik, A. E. Kovalev & N. D. Kushch. Magnetotransport investigation of the low-temperature state of transition $(BEDT\text{-}TTF)_2TIHg(SCN)_4$: evidence for a Peierls-type transition. *J. Phys. I France* **3**, 1187–1199 (1993). URL `http://dx.doi.org/10.1051/jp1:1993264`.

[47] A. G. Lebed, N. N. Bagmet & M. J. Naughton. Magic Angle Effects and Angular Magnetoresistance Oscillations as Dimensional Crossovers. *Phys. Rev. Lett.* **93**, 157006 (2004). URL `http://link.aps.org/doi/10.1103/PhysRevLett.93.157006`.

[48] H. I. Ha, A. G. Lebed & M. J. Naughton. Interference effects due to commensurate electron trajectories and topological crossovers in $(TMTSF)_2ClO_4$. *Phys. Rev. B* **73**, 033107 (2006). URL `http://link.aps.org/doi/10.1103/PhysRevB.73.033107`.

[49] A. G. Lebed & S. Wu. Larkin-Ovchinnikov-Fulde-Ferrell phase in the superconductor $(TMTSF)_2ClO_4$: Theory versus experiment. *Phys. Rev. B* **82**, 172504 (2010). URL http://link.aps.org/doi/10.1103/PhysRevB.82.172504.

[50] Rousseau, R., Doublet, M.-L., Canadell, E., Shibaeva, R. P., Khasanov, S. S., Rozenberg, L. P., Kushch, N. D. & Yagubskii, E. B. Electronic Structure of the α-$(BEDT\text{-}TTF)_2MHg(XCN)_4$ (M K, NH_4; XSe) and Related Phases. Synthesis and Crystal Structure of the New Stable Organic Metal α-$(BEDT\text{-}TTF)_2TlHg(Se_{1-x}S_xCN)_4$ (x25). *J. Phys. I France* **6**, 1527–1553 (1996). URL http://dx.doi.org/10.1051/jp1:1996172.

[51] T. Ishiguro, K. Yamaji & G. Saito. *Organic Superconductors*, Vol. 88 of *Springer Series in Solid-State Sciences* (Springer Verlag Berlin Heidelberg, 1998), 2nd edn.

[52] J. Wosnitza. *Fermi Surfaces of Low-Dimensional Organic Metals and Superconductors*, Vol. 134 of *Springer Tracts in Modern Physics* (Springer Berlin / Heidelberg, 1996). URL http://dx.doi.org/10.1007/BFb0048480. 10.1007/BFb0048480.

[53] H. Mori, S. Tanaka, M. Oshima, G. Saito, T. Mori, Y. Maruyama & H. Inokuchi. Crystal and Electronic Structures of $(BEDT\text{-}TTF)_2M\ Hg(SCN)_4$(M=K and NH_4). *Bull. Chem. Soc. Jpn.* **63**, 2183–2190 (1990).

[54] P. Foury-Leylekian, J.-P. Pouget, Y.-J. Lee, R. M. Nieminen, P. Ordejón & E. Canadell. Density-wave instability in α-$(BEDT\text{-}TTF)_2KHg(SCN)_4$ studied by x-ray diffuse scattering and by first-principles calculations. *Phys. Rev. B* **82**, 134116 (2010). URL http://link.aps.org/doi/10.1103/PhysRevB.82.134116.

[55] M. V. Kartsovnik, D. Andres, S. V. Simonov, W. Biberacher, I. Sheikin, N. D. Kushch & H. Müller. Angle-Dependent Magnetoresistance in the Weakly Incoherent Interlayer Transport Regime in a Layered Organic Conductor. *Phys. Rev. Lett.* **96**, 166601 (2006). URL http://link.aps.org/doi/10.1103/PhysRevLett.96.166601.

[56] M. V. Kartsovnik, P. D. Grigoriev, W. Biberacher & N. D. Kushch. Magnetic field induced coherence-incoherence crossover in the interlayer conductivity of a layered organic metal. *Phys. Rev. B* **79**, 165120 (2009). URL http://link.aps.org/doi/10.1103/PhysRevB.79.165120.

[57] T. Sasaki, N. Toyota, M. Tokumoto, N. Kinoshita & H. Anzai. Transport properties of organic conductor $(BEDT\text{-}TTF)_2KHg(SCN)_4$: I. Resistance and magnetoresistance anomaly. *Solid State Communications* **75**, 93 – 96 (1990). URL http://www.sciencedirect.com/science/article/pii/003810989090348F.

[58] J. S. Brooks, X. Chen, S. J. Klepper, S. Valfells, G. J. Athas, Y. Tanaka, T. Kinoshita, N. Kinoshita, M. Tokumoto, H. Anzai & C. C. Agosta. Pressure effects on the electronic structure and low-temperature states in the α-$(BEDT\text{-}TTF)_2MHg(SCN)_4$ organic-conductor family (M=K, Rb, Tl, NH_4). *Phys. Rev. B* **52**, 14457–14478 (1995). URL http://link.aps.org/doi/10.1103/PhysRevB.52.14457.

[59] P. Foury-Leylekian, S. Ravy, J.-P. Pouget & H. Müller. X-ray study of the density wave instability of α-(BEDT-TTF)$_2$MHg(SCN)$_4$ with M=K and Rb. *Synthetic Metals* **137**, 1271 – 1272 (2003). URL `http://www.sciencedirect.com/science/article/pii/S0379677902010056`. Proceedings of the International Conference on Science and Technology of Synthetic Metals.

[60] Y. Iye, R. Yagi, N. Hanasaki, S. Kagoshima, H. Mori, H. Fujimoto & G. Saito. The Origin of Anomalous Angular Dependent Magnetoresistance Oscillation Effect in α-(BEDT-TTF)$_2$KHg(SCN)$_4$. *Journal of the Physical Society of Japan* **63**, 674–684 (1994). URL `http://jpsj.ipap.jp/link?JPSJ/63/674/`.

[61] T. Sasaki & N. Toyota. Anisotropic galvanomagnetic effect in the quasi-two-dimensional organic conductor α-(BEDT-TTF)$_2$KHg(SCN)$_4$, where BEDT-TTF is bis(ethylenedithio)tetrathiafulvalene. *Phys. Rev. B* **49**, 10120–10130 (1994). URL `http://link.aps.org/doi/10.1103/PhysRevB.49.10120`.

[62] R. H. McKenzie. *cond-mat* 9706235, unpublished (1997).

[63] D. Zanchi, A. Bjeliš & G. Montambaux. Phase diagram for charge-density waves in a magnetic field. *Phys. Rev. B* **53**, 1240–1250 (1996). URL `http://link.aps.org/doi/10.1103/PhysRevB.53.1240`.

[64] T. Helm. *Transport measurements in 214 High-temperature superconductors*. Diplomarbeit, Technische Universität München (2009).

[65] V. N. Zverev, M. V. Kartsovnik, W. Biberacher, S. S. Khasanov, R. P. Shibaeva, L. Ouahab, L. Toupet, N. D. Kushch, E. B. Yagubskii & E. Canadell. Temperature-pressure phase diagram and electronic properties of the organic metal κ-(BETS)$_2$Mn[N(CN)$_2$]$_3$. *Phys. Rev. B* **82**, 155123 (2010). URL `http://link.aps.org/doi/10.1103/PhysRevB.82.155123`.

[66] T. Osada, R. Yagi, A. Kawasumi, S. Kagoshima, N. Miura, M. Oshima & G. Saito. High-field magnetotransport and Fermi-surface topology in the novel quasi-two-dimensional organic conductor bis(ethylenedithiolo)tetrathiafulvalenium mercuric postassium thiocyanate, (BEDT-TTF)$_2$KHg(SCN)$_4$. *Phys. Rev. B* **41**, 5428–5431 (1990). URL `http://link.aps.org/doi/10.1103/PhysRevB.41.5428`.

[67] T. Sasaki, A. G. Lebed, T. Fukase & N. Toyota. Interplay of the spin-density-wave state and magnetic field in the organic conductor α-(BEDT-TTF)$_2$KHg(SCN)$_4$. *Phys. Rev. B* **54**, 12969–12978 (1996). URL `http://link.aps.org/doi/10.1103/PhysRevB.54.12969`.

[68] S. Uji, J. Brooks, M. Chaparala, L. Seger, T. Szabo, M. Tokumoto, N. Kinoshita, T. Kinoshita, Y. Tanaka & H. Anzai. Wave shape of de Haas-van Alphen oscillations and effective mass in the two-dimensional organic conductor α-(BEDT-TTF)$_2$KHg(SCN)$_4$. *Solid State Communications* **100**, 825 – 830 (1996). URL `http://www.sciencedirect.com/science/article/pii/S0038109896005157`.

[69] A. A. House, W. Lubczynski, S. J. Blundell, J. Singleton, W. Hayes, M. Kurmoo & P. Day. The low-temperature phase of α-(BEDT-TTF)$_2$KHg(SCN)$_4$: II. Pressure dependence of the Shubnikov - de Haas oscillations. *Journal of Physics: Condensed Matter* **8**, 10377 (1996). URL `http://stacks.iop.org/0953-8984/8/i=49/a=027`.

[70] P. Christ, W. Biberacher, H. Müller & K. Andres. Magnetization measurements on α-(BEDT-TTF)$_2$KHg(SCN)$_4$ [where BEDT-TTF is bis(ethylenedithio)tetrathiafulvalene]. *Solid State Communications* **91**, 451 – 455 (1994). URL `http://www.sciencedirect.com/science/article/pii/0038109894907846`.

[71] P. Christ, W. Biberacher, H. Müller, K. Andres, E. Steep & A. Jansen. High field magnetization measurements on α-(BEDT-TTF)$_2$KHg(SCN)$_4$. *Synthetic Metals* **70**, 823 – 824 (1995). URL `http://www.sciencedirect.com/science/article/pii/037967799402664K`. Proceedings of the International Conference on Science and Technology of Synthetic Metals.

[72] A. Kovalev, M. Kartsovnik, R. Shibaeva, L. Rozenberg, I. Schegolev & N. Kushch. Angular magnetoresistance oscillations in the organic conductor α-(BEDT-TTF)$_2$KHg(SCN)$_4$ above and below the phase transition. *Solid State Communications* **89**, 575 – 578 (1994). URL `http://www.sciencedirect.com/science/article/pii/003810989490166X`.

[73] A. G. Lebed & N. N. Bagmet. Nonanalytical magnetoresistance, the third angular effect, and a methodto investigate Fermi surfaces in quasi-two-dimensional conductors. *Phys. Rev. B* **55**, R8654–R8657 (1997). URL `http://link.aps.org/doi/10.1103/PhysRevB.55.R8654`.

[74] D. Andres, M. Kartsovnik, W. Biberacher, K. Neumaier, I. Sheikin, H. Müller & N. Kushch. Field-induced charge-density-wave transitions in the organic metal α-(BEDT-TTF)$_2$KHg(SCN)$_4$ under pressure. *Low temperature physics* **37**, 959–969 (2011).

[75] J. I. Oh & M. J. Naughton. Magnetic Determination of H_{c2} under Accurate Alignment in (TMTSF)$_2$ClO$_4$. *Phys. Rev. Lett.* **92**, 067001 (2004). URL `http://link.aps.org/doi/10.1103/PhysRevLett.92.067001`.

[76] D. Andres, M. V. Kartsovnik, P. D. Grigoriev, W. Biberacher & H. Müller. Orbital quantization in the high-magnetic-field state of a charge-density-wave system. *Phys. Rev. B* **68**, 201101 (2003). URL `http://link.aps.org/doi/10.1103/PhysRevB.68.201101`.

[77] A. E. Kovalev, S. Hill & J. S. Qualls. Determination of the Fermi velocity by angle-dependent periodic orbit resonance measurements in the organic conductor $\alpha - (\mathrm{BEDT-TTF})_2\mathrm{KHg(SCN)}_4$. *Phys. Rev. B* **66**, 134513 (2002). URL `http://link.aps.org/doi/10.1103/PhysRevB.66.134513`.

[78] M. V. Kartsovnik, P. D. Grigoriev, W. Biberacher, N. D. Kushch & P. Wyder. Slow Oscillations of Magnetoresistance in Quasi-Two-Dimensional Metals. *Phys. Rev. Lett.* **89**, 126802 (2002). URL `http://link.aps.org/doi/10.1103/PhysRevLett.89.126802`.

[79] M. Lang & J. Müller, *Superconductivity*. K. H. Bennemann & J. B. Ketterson (eds.), chap. Organic Superconductors, 1155–1223 (Springer Berlin Heidelberg, 2008). URL `http://dx.doi.org/10.1007/978-3-540-73253-2_20`.

[80] S. Onari, R. Arita, K. Kuroki & H. Aoki. Phase diagram of the two-dimensional extended Hubbard model: Phase transitions between different pairing symmetries when charge and spin fluctuations coexist. *Phys. Rev. B* **70**, 094523 (2004). URL `http://link.aps.org/doi/10.1103/PhysRevB.70.094523`.

[81] J. Merino & R. H. McKenzie. Superconductivity Mediated by Charge Fluctuations in Layered Molecular Crystals. *Phys. Rev. Lett.* **87**, 237002 (2001). URL `http://link.aps.org/doi/10.1103/PhysRevLett.87.237002`.

[82] K. Maki, N. Schopohl & H. Won. D-wave superconductor in high magnetic fields. *Physica B: Condensed Matter* **204**, 214 – 221 (1995). URL `http://www.sciencedirect.com/science/article/pii/092145269400266X`.

Acknowledgments

At the end of this work I would like to thank all the poeple, who helped me to make this work possible.

I especially want to express my gratitude to:

- Prof. Dr. Rudolf Gross, for giving me the possibility of doing this work at the Walther-Meißner-Institut.
- Dr. Mark Kartsovnik and Dr. Werner Biberacher, for introducing me to the subject of organic superconductors, for sharing their knowledge with me and for always advising me when needed.
- Toni Helm, for his advice especially in the subjects of LabView and LaTeX.
- Sebastian Jakob, for establishing the measurement setup during his diploma work period and for helping us with advice even though having left the institute four years ago.
- Prof. Dr. Vladimir N. Zverev, for performing the effective cyclotron mass experiment together with me.
- Joachim Geismann, for building the new gas-handling system for our dilution refrigerator.
- Dr. Karl Neumaier, for his advising us how to operate the dilution fridge.
- the technical staff of the WMI, for their help in the case of problems with the measurement equipment, especially to Ulrich Guggenberger, who repaired our magnet power supplies several times.
- the other students and scientists at the WMI, for the nice working atmosphere.
- Sebastian Schulteß and David Müller, for proofreading this work.

In particular, I want to thank my parents, for giving me the chance to study physics and for their support in the course of my study.

Erklärung

des Diplomanden

Name:

Vorname:

Mit der Abgabe der Diplomarbeit versichere ich, dass ich die Arbeit selbständig verfasst und keine anderen als die angegebenen Quellen und Hilfsmittel benutzt habe.

....

(Ort, Datum) (Unterschrift)